RESEARCH MEMORANDUM

ANALYSIS OF PERFORMANCE OF FOUR SYMMETRICAL-DIAGRAM-TYPE SUBSONIC INLET-STAGE AXIAL-FLOW COMPRESSORS

By Robert J. Jackson

Lewis Flight Propulsion Laboratory
Cleveland, Ohio

NATIONAL ADVISORY COMMITTEE
FOR AERONAUTICS

WASHINGTON

January 20, 1954

ERRATA NO. 1

NACA RM E53K03

ANALYSIS OF PERFORMANCE OF FOUR SYMMETRICAL-DIAGRAM-TYPE SUBSONIC INLET-STAGE AXIAL-FLOW COMPRESSORS

By Robert J. Jackson

January 20, 1954

Figure 14(b). The abscissa scale should read from -4° to 28°.

Figure 20. The symbol for 115° design speed ▽ should be added to the key.

Figure 20(b). The mean radius and hub region labels should be transposed.

Figure 27(a) "After guide vanes." The following curve should be substituted for the curve for a peak efficiency of 21.51:

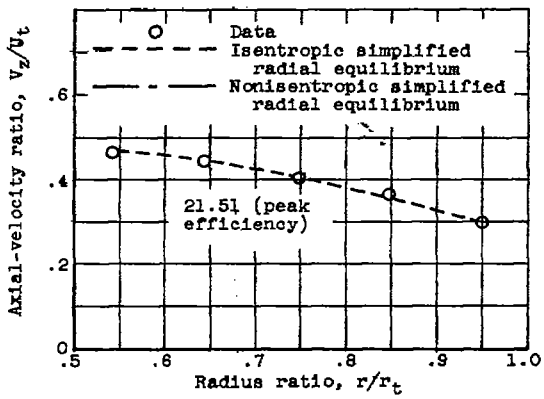

Figure 27(d) "After rotor." The following curve should be substituted for the curve for a peak efficiency of 25.17:

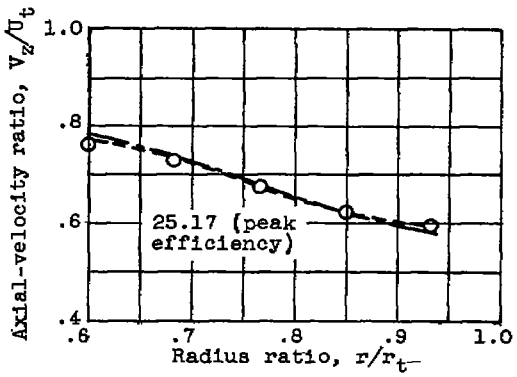

NACA-Langley - 3-2-54 - 325

NATIONAL ADVISORY COMMITTEE FOR AERONAUTICS

RESEARCH MEMORANDUM

ANALYSIS OF PERFORMANCE OF FOUR SYMMETRICAL-DIAGRAM-TYPE SUBSONIC INLET-STAGE AXIAL-FLOW COMPRESSORS

By Robert J. Jackson

SUMMARY

An investigation of four axial-flow single-stage compressors having a hub-tip radius ratio of 0.5 was made with the following objectives: (1) evaluation of the analytical conclusion that the most suitable use for the symmetrical-velocity-diagram design with constant stagnation enthalpy is for high-specific-weight-flow designs, (2) the comparison of blade-element turning angle and loss data with corresponding cascade data, and (3) checking the validity of the simplified-radial-equilibrium equation.

For a given Mach number limit, high pressure ratio required a design assumption of low specific weight flow (low design axial-velocity ratio $(V_z/U_t)_h$). Because of the action of radial equilibrium, this design assumption resulted in high rotor-tip-region rates of diffusion (as measured by the D factor) with consequent high losses and low peak efficiencies. Therefore the most suitable use for the symmetrical-velocity-diagram was for lower-pressure-ratio and higher-specific-weight-flow designs.

For the available rotor blade-element data, a correlation for a given solidity was obtained among compressor and cascade-predicted deviation angles as functions of D factor.

For the low-D-factor design (design 4) fairly good correlation was obtained between cascade-predicted and rotor turning angles as functions of angle of attack.

A correlation of tip-region rotor relative-total-pressure losses for designs 1 and 4 as functions of D factor was obtained for D factors exceeding approximately 0.55. The cascade-predicted losses did not correlate with tip-region rotor losses because the latter are influenced by other factors in addition to blade-suction-surface flow separation.

The over-all range of flow coefficient (or weight flow) for the lowest-axial-velocity design at a given value of efficiency was limited by the high tip-region total-pressure losses caused by high D factors

and the high rate of change of angle of attack with flow coefficient imposed by high guide-vane turning.

The available stator data represented the low-D-factor type of design. The stator blade-element minimum losses varied only slightly with radius and between the two designs for which data were available.

The available data indicated that the assumption of simplified radial equilibrium was a valid one. For most of the cases investigated, the axial-velocity profiles obtained from the calculation neglecting entropy gradient agreed fairly well with the data at the rotor inlet and outlet. In order to obtain good agreement between the calculated axial velocities and the data downstream of the stators, it was necessary to include the effect of the entropy gradient. A small discrepancy remained between the predicted and measured velocities near the hub, which was probably caused by the omission of the radial acceleration terms from the radial-equilibrium equation.

INTRODUCTION

Blade-element efficiency analysis has indicated that the optimum velocity diagram for an axial-flow compressor stage is symmetrical (ref. 1). This analysis was based on assumptions of constant axial velocity and no radial flow. Consideration of the radial variation of velocities, as prescribed by simplified radial equilibrium requirements, indicated that, for given limitations of a loading parameter σC_L and relative inlet Mach number, the average stage pressure ratio and specific weight flow would be higher for the symmetrical velocity diagram than for the free-vortex design.

The analysis of reference 1 also indicated a disadvantage of the symmetrical-velocity-diagram and constant-stagnation-enthalpy design, namely, that the axial velocity may become very low or actually reverse near the tip, especially after the rotor, for low-weight-flow designs. This effect could lead to a flow separation along the outer wall. The analysis therefore indicated that the most suitable use for the symmetrical velocity diagram with constant stagnation enthalpy is for high-specific-weight-flow designs.

An investigation of four symmetrical-diagram-type axial-flow compressor stages has been made at the NACA Lewis laboratory to determine the effects on efficiency as design weight flow is increased in order to evaluate experimentally the general discussion of reference 1. Four axial-flow subsonic single-stage compressors having a hub-tip radius ratio of 0.5 were designed, built, and investigated. The form of the design equations made it convenient to use the ratio of axial velocity at the hub to tip speed $(V_z/U_t)_h$ as the independent variable among the four designs; the design values of $(V_z/U_t)_h$ for designs 1 through 4 were, respectively, 0.6, 0.7, 0.8, and 0.9. For the given limits of

σC_L (0.77) and relative inlet Mach number (approximately 0.7), these increasing values of design $(V_z/U_t)_h$ resulted in successively increasing design weight flow and decreasing design pressure ratio and tip speed.

A parallel objective of the investigation was the comparison of blade-element turning angle and loss data with corresponding cascade data. Such comparisons would be expected to indicate where cascade data satisfactorily predict compressor performance and where other design methods must be used.

Finally, the validity of the simplified-radial-equilibrium equation was investigated. The analysis of tip-region axial-velocity characteristics for low-weight-flow designs (ref. 1) was based on this equation; it was also used in the design of the compressors of the present investigation.

The four compressors were investigated, where possible, over a range of speeds and weight flows in two configurations: guide vanes and rotor (referred to as rotor investigations); and guide vanes, rotor, and stator (referred to as full-stage investigations).

Preliminary results of the investigations of designs 1 and 2 have been presented in references 2 and 3.

COMPRESSOR DESIGN AND CONFIGURATION

Design calculations. - At the time the compressors were designed, the best available information indicated that some constant value of the parameter σC_L represented the loading limit for a cascade of blades. For a symmetrical velocity diagram at all radii and constant enthalpy addition, this limitation in σC_L was reached at the rotor hub where the required turning was greatest. For the 65-(12)10 airfoil section used for the compressor blading, the limiting value assigned for σC_L was 0.77.

For the symmetrical velocity diagram, the change in tangential velocity across the rotor was computed as follows:

$$\left(\frac{\Delta V_\theta}{U_t}\right)_h = \frac{\sigma C_L}{2} \sqrt{\left(\frac{V_{z,1}}{U_t}\right)_h^2 + \frac{1}{4}\left(\frac{r_1}{r_t}\right)_h^2} \qquad (1)$$

(This equation was derived in ref. 4; symbols are defined in appendix A.)

[redacted]

The assigned values of $(V_{z,1}/U_t)_h$ for designs 1 to 4, respectively, were 0.6, 0.7, 0.8, and 0.9. A radial vortex distribution of $\Delta V_\theta/U_t$, defined as follows,

$$\frac{d}{dr}\left(\frac{U\Delta V_\theta}{U_t^2}\right) = 0$$

established the inlet tangential relative and absolute velocity ratios at all radii.

The radial distribution of inlet axial-velocity ratio V_z/U_t was calculated from the simplified-radial-equilibrium equation in the following integrated form (ref. 5):

$$\frac{V_{z,1}}{U_t} = \sqrt{\left(\frac{V_z}{U_t}\right)_h^2 + \frac{1}{2}\left[\left(\frac{r}{r_t}\right)_h^2 - \left(\frac{r}{r_t}\right)^2\right] + \left(\frac{r}{r_t}\right)_h \left(\frac{\Delta V_\theta}{U_t}\right)_h \ln\frac{r}{r_h}} \qquad (2)$$

For the preliminary calculations the flow passage was assumed to be an untapered annulus and the axial variation of axial velocity was assumed zero at any given radius. From the relative inlet Mach number limit (0.725 for design 1; 0.7 for the other designs) and the assumed adiabatic efficiency (0.89), the weight flow and the total density ratio across the stage were calculated as follows:

$$\frac{H_1}{U_t^2} = \frac{\left(1 + \frac{\gamma-1}{2} M_{1,h}'^2\right)\left(\frac{V_1}{U_t}\right)_h^2 + \frac{U\Delta V_\theta}{U_t^2}}{(\gamma-1)\, M_{1,h}'^2} \qquad (3)$$

$$W_1 = 2\pi\rho_{1,T} r_t^2 U_t \int_{\frac{r_{1,h}}{r_t}}^{1.0} \frac{V_{z,1}}{U_t}\frac{r_1}{r_t}\left[\frac{\frac{H_1}{U_t^2} - \frac{1}{2}\left(\frac{V_1}{U_t}\right)^2}{\frac{H_1}{U_t^2}}\right]^{\frac{1}{\gamma-1}} d\left(\frac{r_1}{r_t}\right) \qquad (4)$$

[redacted]

$$\left(\frac{\rho_3}{\rho_1}\right)_T = \frac{\left(1 + \eta \frac{U\Delta V_\theta / U_t^2}{H_1/U_t^2}\right)^{\frac{\gamma}{\gamma-1}}}{1 + \frac{U\Delta V_\theta / U_t^2}{H_1/U_t^2}} \tag{5}$$

A trial-and-error solution for $r_{3,h}/r_t$ was required so that the continuity condition would be satisfied:

$$W_1 = W_3 = 2\pi\rho_{3,T} r_t^2 U_t \int_{\frac{r_{3,h}}{r_t}}^{1.0} \frac{V_{3,z}}{U_t} \frac{r_3}{r_t} \left[\frac{\frac{H_3}{U_t^2} - \frac{1}{2}\left(\frac{V_3}{U_t}\right)^2}{\frac{H_3}{U_t^2}} \right]^{\frac{1}{\gamma-1}} d\left(\frac{r_3}{r_t}\right) \tag{6}$$

This design process was repeated for a following stage; this resulted in three points on the hub contour: $r_{1,h}$, $r_{3,h}$, and the hub radius after the second stage. A smooth curve faired through the three points established the hub shape. (Only the inlet-stage designs were actually built and investigated.) At the time these stages were designed, very few cascade data were available. Therefore, the blade angles were calculated by means of the Kantrowitz and Daum equation (ref. 6):

$$\epsilon = K(\alpha - \alpha_0)$$

where K (assumed to be 0.9) was a function of solidity and relative inlet air angle, and the angle of attack for an airfoil at zero lift α_0 equaled -8.28° for the 65-(12)10 blade profile. For 65-series airfoils, the theoretical angle of attack at zero lift is $\alpha_0 = -\frac{57.3}{2\pi} C_L$ (ref. 7), where C_L is the lift coefficient of an isolated airfoil at zero angle of attack. Experimental data indicated that the theoretical value of C_L should be multiplied by a factor 0.8 and that the slope of the lift curve for a cascade of airfoils was 0.116. On this basis, α_0 for the 65-(12)10 airfoil equaled -8.28°. The extent to which K decreased for the low solidities and high inlet angles near the tip was not known; an

approximate correction for this reduced K was made by reducing the calculated blade angles near the tip by small amounts. The magnitude of this modification at the tip was greatest for design 1, which had the highest relative inlet angle.

Compressor configurations. - The flow angles required at the rotor inlet were provided by 40 sheet metal guide vanes 1/16 inch thick. These vanes had a constant-radius-of-curvature circular-arc camber line. The required turning was obtained by appropriate adjustment of the chord length.

In figure 1 are presented the details of the rotor-and-stator-blade configurations for the four designs: blade-angle setting ξ, solidity σ, and radius ratio r/r_t are tabulated. Also presented are the design distributions of absolute inlet air angle (guide-vane turning) β, guide-vane camber φ, relative inlet air angle β', and rotor-inlet axial-velocity ratio V_z/U_t. The NACA 65-(12)10 blade section with a constant chord of 1.31 inches was used for all rotor and stator blades. The hub-tip radius ratio at the rotor inlet was 0.5 and the rotor-tip diameter was 14 inches for all designs.

It will be noted that the rotor and stator blade angles for design 1 differed more than did the corresponding angles for the other designs (fig. 1). This was a consequence of an error in blade angle made during fabrication of the rotor blades. The error was discovered subsequent to the publication of reference 2 and amounted to a discrepancy of as much as 7° between the design rotor-blade-angle settings and the actual rotor-blade angles. The stator-blade angles were correct. At the time reference 2 was written, no inlet stage data were available for comparison. Later, when such data became available, it was found that the energy addition and turning-angle characteristics did not correlate with the new data. The blade angles of all the blade rows concerned were checked and the error for the rotor of design 1 was discovered. All other blade angles were correct.

APPARATUS AND PROCEDURE

Experimental setup. - A schematic diagram of the experimental setup is shown in figure 2. The compressor was driven by a 1500-horsepower dynamometer. Room air was drawn through a flat-plate orifice into a large depression tank. From the depression tank the air passed through a bellmouth inlet into the compressor, then through a large collector to the laboratory altitude exhaust system. The desired inlet pressure and weight flow were set by means of valves located between the orifice tank and the depression tank, and between the collector and the exhaust system.

Instrumentation. - The location of the measuring stations is indicated in figure 3. For the rotor investigations, flow measurements were taken approximately 0.2 chord length upstream of the rotor blades and 0.6 chord length downstream of the rotor blades. For the full-stage investigations, measurements were taken 0.2 chord length upstream of the rotor blades, 0.55 chord length downstream of the rotor blades, and 0.6 chord length downstream of the stator blades. Data were taken at five radial stations a, b, c, d, and e, which were located nominally at the centers of five equal radial increments across the annular passage at the various axial stations. (This method of locating the radial stations was not held exactly for all investigations; otherwise, a new set of stagnation-temperature probes would have been required for each design in order to fit the different passage depths downstream of the stage.)

The instrumentation used for the rotor investigations was described in detail in reference 8. For the full-stage investigation, a summary of the number of probes and type of instrumentation used is presented in the following table. It should be noted that, because of the negligible velocities in the depression tank, the depression-tank static pressure p_0 as measured by wall taps was assumed to equal the depression-tank stagnation pressure P_0.

Axial station	Temperature	Stagnation pressure	Static pressure	Angle
Inlet orifice	Four iron-constantan thermo-couples	Barometer reading	Two wall static-pressure taps	
Depression tank, 0	Four iron-constantan thermo-couples	Two wall static-pressure taps	Two wall static-pressure taps	
Upstream of rotor, 1		$P_1 = P_0$ minus guide vane loss (obtained from circumferential surveys, ref. 8)	One wedge-type static-pressure probe (fig. 4(a))	One claw total-head-type yaw-measuring probe
Downstream of rotor, 2		(a)	One wedge-type static-pressure probe	One claw total-head-type yaw-measuring probe
Downstream of stator, 3	Four 5-tip double-stagnation-type stagnation-temperature rakes (fig. 4(c))	Five 19-tube stagnation-pressure rakes (fig. 4(d))	One wedge-type static-pressure probe	One claw total-head-type yaw-measuring probe

[a]Maximum pressure indicated by 19-tube stagnation-pressure rake was taken to be P_2; arithmetical average of 19 readings was taken to be P_3.

[redacted]

Radial surveys were made with the static-pressure and yaw-measuring probes (figs. 4(a) and (b)). There were some exceptions to this scheme of full-stage instrumentation; in particular, no measurements at axial station 2 were made for the investigations of designs 1 and 2.

Experimental procedure. - The following table summarizes the speeds investigated (in terms of percent design speed) for the rotor and the full-stage configurations.

Design number	Design tip speed, ft/sec	Percent design speed	
		Rotor investigations	Full-stage investigations
1	1104	100, 110	50, 100, 110
2	938	100	50, 75, 100 120, 130
3	823		30, 50, 75 100, 120, 135
4	743	50, 75, 100	50, 75, 110, 115

Certain of the data proved to be invalid. It is believed that the guide-vane losses for design 4 were not sufficiently accurate for the isolation of the rotor blade-element relative total-pressure losses at 50 percent design speed. At the low power input for this speed, the relative total-pressure ratio $(P_2/P_1)'$ is very sensitive to slight errors in stagnation pressure. Calculations, based on typical values of pressure, temperature, and relative Mach number encountered at 50 percent speed, indicate that an error in P_1 of 0.04 inch of mercury would cause an error of approximately 50 percent in the calculated value of the total-pressure-loss parameter $\bar{\omega}$. In contrast, the same percentage error in $\bar{\omega}$ at design speed would require an error of 0.2 inch of mercury in P_1.

For the design 2 full-stage investigations at 50 and 75 percent design speed, the data were measured with a different scheme of instrumentation from that described in the section Instrumentation and utilized for all the other full-stage investigations presented herein. In particular, the stagnation-temperature probes were of a design which proved to be very sensitive in calibration to the total-pressure level. It is believed that the design-speed data for design 2 provide a more reliable

indication of the peak efficiency than do the low-speed data. The design 2 rotor investigation also utilized the stagnation-temperature probes which varied in calibration with the total pressure; therefore, the data are inadequate for a satisfactory rating of the rotor efficiency. These data are probably accurate enough for the calculation of velocity diagrams and are used only for this purpose.

The flow angles after stators for the design 3 full-stage investigations at 120 and 135 percent design speed and the temperature-rise data for several high-flow points for the design 4 full-stage investigation at 50 percent speed were apparently invalid because of troubles encountered in the testing procedure.

Data from rotor investigations were relatively meager because of several blade failures. These are tabulated as follows:

Design number	Configuration investigated	Percent design speed	Type of failure and damage
1	Rotor	110	Rig failure; all blades wiped out.
2	Full stage	130	Stator blade broke off and damaged rotor blade trailing edges. Several rotor blades cracked.
3	Full stage	about 75 (Failure occurred while shutting down from 135 percent speed)	All blades wiped out. Suspected cause, fatigue failure.
4	Full stage	Very low flows at about 50 percent speed	One stator blade broke off. All blades cracked. Probable cause, vibratory stress excited by rotating stall (ref. 9).

Although the blade failures experienced with designs 2 and 3 occurred at high speed, it is suspected that their primary cause was the same as for design 4. Designs 2 and 3 were both investigated under stall conditions prior to the high-speed tests.

The investigation reported in reference 9 was conducted on design 4 subsequent to the accumulation of the data reported herein.

RESULTS AND DISCUSSION

Over-All Performance

Pressure ratio and efficiency. - The over-all performance of each design, for the full-stage investigations tabulated in the section Experimental procedure, is presented in figure 5 as plots of average total-pressure ratio P_3/P_0 and average adiabatic temperature-rise efficiency η against corrected weight flow $W\sqrt{\theta}/\delta$. The calculation of these rating parameters is outlined in appendix B. The following table summarizes some of the main features of this performance for the full-stage configurations at their respective design speeds:

Design number	Design tip speed, ft/sec	$\left(\frac{V_z}{U_t}\right)_{h,des}$	Peak pressure ratio point			Peak efficiency point		
			P_3/P_0	η	$W\sqrt{\theta}/\delta$	P_3/P_0	η	$W\sqrt{\theta}/\delta$
1	1104	0.6	1.250	0.86	21.2	1.235	0.86	22.2
2	938	.7	1.220	.87	24.0	1.215	.87	24.5
3	823	.8	1.195	.89	24.5	1.190	.89	25.5
4	743	.9	1.155	.87	24.5	1.150	.89	26.5

The trends of decreasing pressure ratio and increasing weight flow at the peak efficiency point for the successive designs were expected from the design calculations; however, the corresponding decrease in peak pressure ratio, although not unexpected, could not be predicted with certainty in the absence of off-design-point calculations. An appreciable increase in peak efficiency is indicated for the high-axial-velocity designs (designs 3 and 4). This efficiency trend experimentally verifies the result of the analysis of reference 1 that the symmetrical velocity diagram is more suitable for high-specific-weight-flow designs than for designs of the low-specific-weight-flow and high-pressure-ratio type.

Dimensionless over-all performance. - It would be of interest to study the performance of the four compressors in a dimensionless form so that the potentialities of the velocity diagrams may be evaluated without regard for limitations on the performance of these particular compressors that may be imposed by the actual blading that is used (Mach number effects, for instance). The over-all performance of the four compressors is presented in figure 6 as plots of average ideal dimensionless enthalpy addition $\Delta H_{id}/U_t^2$ and average adiabatic temperature-rise efficiency η against the flow coefficient $(V_z/U_t)_{av}$. (The calculation of these rating parameters is given in appendix B.) The discussions and comparisons that follow refer mainly to the correlated curves for the data which fall approximately within design Mach number limits (50 to 115 percent design speed).

The curves reveal that the peak dimensionless ideal enthalpy addition $\Delta H_{id}/U_t^2$ increases as design axial-velocity ratio $(V_z/U_t)_h$ increases. The values for designs 1 to 4 are about 0.17, 0.20, 0.24, and 0.23, respectively; apparently, the peak value of $\Delta H_{id}/U_t^2$ would occur for $(V_{z,h}/U_t)_{des}$ between 0.8 and 0.9. The reason for increasing design values of $\Delta H_{id}/U_t^2$ can be seen from a slight manipulation of equation (1)

$$\left(\frac{\Delta H_{id}}{U_t^2}\right)_{des} = \eta_{des} \frac{r_{1,h}}{r_t} \frac{\sigma C_L}{2} \sqrt{\left(\frac{V_{z,1}}{U_t}\right)_h^2 + \frac{1}{4}\left(\frac{r_1}{r_t}\right)_h^2}$$

The only variable in this equation for the different designs is the axial-velocity ratio $(V_z/U_t)_h$. Obviously, $(\Delta H_{id}/U_t^2)_{des}$ increases as $(V_{z,1}/U_t)_h$ increases and it is reasonable to expect the peak values of $\Delta H_{id}/U_t^2$ to follow the same trend.

The decreasing peak pressure ratio at a given percent of design speed for the high-axial-velocity designs (fig. 5) is caused by the lower design speed assigned to these designs. The fact that for a given relative Mach number limit the design speed must decrease as axial velocity increases is easy to visualize: an increase in axial Mach number must be balanced by a decrease in the relative tangential Mach number, which requires a decrease in compressor Mach number (ratio of wheel speed to velocity of sound).

[redacted]

The efficiency curves of figure 6 indicate an increasing range of flow coefficient as design axial-velocity ratio $(V_{z,1}/U_t)_h$ is increased. The following table summarizes the characteristics of the flow-coefficient range at the subcritical Mach number speeds for an efficiency of at least 0.80.

Design number	$(V_{z,1}/U_t)_{h,des}$	Range of $(V_{z,1}/U_t)_{av}$
1	0.6	0.117
2	.7	.205
3	.8	.275
4	.9	.330

For subsonic Mach numbers, weight flow increases as axial velocity increases; therefore, increased range of flow coefficient corresponds, for a given tip speed, to increased range of weight flow.

The study of the over-all performance in dimensionless form has indicated some potentialities of the high-axial-velocity type of velocity diagram. For such a diagram, high pressure ratio can be combined with high weight flow and with a wide efficient range of weight flow, providing the blading is tolerant of the consequent high relative Mach numbers. The investigations of reference 10 indicate that such blade sections are available.

Velocity diagrams. - The consequences of the design assumptions of the axial-velocity ratio $(V_{z,1}/U_t)_h$ for the four designs in terms of the velocity diagram geometry may be seen in figure 7 wherein are shown velocity diagrams from the data of the peak efficiency points at design speed. Numerical values of velocities and flow angles are tabulated in figure 7(e).

On the basis of two-dimensional cascade data, the relative inlet angle is the only variable among the four designs that would affect the performance of a given blade element. (At a given radius, solidity and camber are the same for all designs.) The diagrams show the decrease in

inlet angles (both relative and absolute) for the successive designs, and also show that this decrease is greatest for design 2. The magnitude of this decrease is more clearly shown in figure 8, where relative inlet air angle β_1' is plotted against rotor angle of attack α_1 for stations a, c, and e. (Fig. 8 is not a plot of data; the relation between β_1' and α_1 is simply $\beta_1' = \alpha_1 + \xi_1$, where ξ_1 is the rotor blade angle.) The figure shows that for a given angle of attack, the relative inlet angle for design 1 is much higher than the relative inlet angles for the other designs. Another important feature of the flow is the axial-velocity ratio $V_{z,2}/V_{z,1}$. For design 1, figure 7(a) shows a large decrease in axial velocity for station a; for design 4 (fig. 7(d)) there is very little reduction in axial velocity at the tip-region measuring station. For a quantitative comparison, the values of axial-velocity ratio $V_{z,2}/V_{z,1}$ are plotted against corrected weight flow $W\sqrt{\theta}/\delta$ in figure 9 for designs 1 and 4 at design speed. For design 1, a considerable shift in flow towards the hub is indicated by the large decrease in axial velocity near the tip and increase near the hub. The possible consequences of such a radial shift in flow were discussed in reference 8. Briefly, the indication is that the blade surface local pressure gradients may become excessive and lead to premature flow separation with resulting high losses. For design 4, the axial-velocity ratios at the three radial stations are within the range from 0.96 to 1.08 except at flows in the tip-stall region, which indicates that only a slight radial shift in flows exists at unstalled conditions.

Blade-Element Performance

A study of the blade-element performance is required for analysis of the following trends: (1) increasing peak efficiency as design axial-velocity ratio $(V_{z,1}/U_t)_h$ is increased, and (2) increasing efficient weight-flow (or flow-coefficient) range.

The rotor investigations of designs 1 and 4 supplied the available rotor blade-element performance; the stator blade-element performance was obtained from the full-stage investigations of designs 3 and 4. In order to isolate the rotor-blade-row performance, inlet guide-vane losses were measured.

Inlet guide-vane loss. - The guide vanes were set at zero incidence for all investigations; therefore, at a given radius, the dimensionless total-pressure loss $\bar{\omega}$ (ref. 11) did not vary significantly with speed or weight flow. The total-pressure loss $\bar{\omega}$ for designs 1 and 4 is presented in figure 10 as a function of radius ratio r/r_t.

[redacted]

The dimensionless total-pressure loss $\bar{\omega}$ for designs 1 and 4 is practically the same for each design (approximately 0.060) except near the tip. At the tip measuring station, the higher-turning guide vane has the higher loss, the respective values being 0.17 and 0.13. The performance calculations showed that consideration of these guide-vane losses affected calculated rotor angles of attack by 0.5° to 1.5° and peak element efficiencies by as much as 5 percentage points, thus emphasizing the necessity of isolating the performance of each blade row.

Rotor blade-element performance. - The blade-element data are presented for the rotors in terms of turning angles and losses against angle of attack. These data are then correlated among themselves and with cascade data by application of a blade-loading parameter.

The available rotor blade-element turning-angle and loss characteristics measured at radial stations a, c, and e are presented for designs 1 and 4. As discussed in the section Experimental procedure, blade failures prevented the rotor investigation of designs 2 and 3.

Relative inlet Mach number is plotted against rotor angle of attack in figure 11 so that the possibility of Mach number effects on losses and turning angle can be analyzed. Figure 11 shows that the highest value of relative inlet Mach number for the investigation of design 1 was 0.79 (110 percent design speed, station a) and for design 4 was 0.71 (100 percent design speed, station e).

Turning angles: Turning angles ϵ_1 for the speeds investigated are plotted against angle of attack α_1 in figure 12 for designs 1 and 4.

For design 1 at the tip-region measuring station, turning angle decreases as angle of attack increases above a value of approximately 2°. For the other measuring stations, turning angle increases with angle of attack for the angle-of-attack range investigated, and no break-off is noted for either of the two curves.

For design 4, the tip-region turning-angle curve differs markedly from the curve for design 1. Turning angle increases almost linearly up to an angle of attack of about 8°. No complete break-off (where the slope becomes negative) is noted for the range of angle of attack investigated.

The highest relative Mach number obtained for the rotor investigation of design 4 was about 0.70 (fig. 11); this level of Mach number has no apparent effect on turning angle.

Comparisons of rotor turning angles with cascade data: A comparison of the rotor turning angle data for designs 1 and 4 is presented in figure 13. The curves drawn through the data points of figure 12 are reproduced in figure 13. Also presented are cascade predictions of the turning angles as interpolated from the data of reference 12.

Figure 13 brings out clearly the dissimilarities between the turning angle characteristics of designs 1 and 4 for the tip-region measuring station (station a). A comparison with cascade data is indicated in order to determine whether this difference in turning-angle characteristics can be accounted for by cascade predictions.

The cascade-predicted turning angles for designs 1 and 4 that are plotted in figure 13 differ appreciably at station a. This difference is a consequence of the fact that at a given angle of attack, the relative inlet angle for design 1 is 28.2° higher than for design 4 (fig. 8). However, the predicted reduction in turning angle for design 1 compared to design 4 does not approach the magnitude of the actual decrease. Also, the cascade results indicate a peak in the turning-angle curve at an angle of attack of about 12° to 14°, whereas the compressor data indicated a break-off point at a 2° angle of attack.

For design 4, the cascade data predict very well the slope of the curve at station a, although there is an indicated discrepancy of 2° to 3° between the compressor data and the cascade data. For the two designs at stations c and e, the cascade data indicate progressively less difference in predicted turning angle, and the compressor turning-angle curves check the cascade data fairly well in slope and ordinates (within 3°, except for design 1, station e at low angles of attack).

Total-pressure losses: The relative total-pressure-loss parameter $\bar{\omega}$ for designs 1 and 4 is plotted against angle of attack α_1 in figure 14. The 50-percent-design-speed total-pressure-loss parameters for design 4 are not presented here for reasons discussed in the section Experimental procedure.

For design 1 the minimum total-pressure loss $\bar{\omega}$ decreases from about 0.150 near the tip to about 0.015 near the hub. Partly because of this decrease in minimum loss, and partly because the curves are flatter near the hub, the range of angle of attack for a given loss increases from the tip to the hub.

For design 4, the minimum total-pressure loss $\bar{\omega}$ decreases from about 0.060 near the tip to about 0.010 near the hub. At each measuring station the minimum loss is appreciably lower than the corresponding loss

for design 1. Also, at each station, the angle-of-attack range for a given loss exceeds the corresponding range for design 1; in fact, it is apparent that the complete range of angle of attack was not investigated at station e.

Comparison of rotor loss with cascade-predicted loss: A comparison of rotor relative-total-pressure losses for designs 1 and 4 is presented in figure 15. The curves drawn through the data points of figure 14 are reproduced in figure 15 along with the cascade-predicted values of $\bar{\omega}$ computed from the data of reference 12.

The curves of figure 15 clearly reveal the differences between the two designs in minimum loss and in angle-of-attack range for a given loss.

An approximate agreement between the rotor losses and the cascade-predicted losses is obtained only at station e. At station a, the minimum measured rotor losses for designs 1 and 4 are approximately 10 times the corresponding cascade values.

The reasons for the lack of correlation between the compressor and cascade turning-angle and loss curves for design 1 must be involved with the markedly three-dimensional nature of the flow at the tip region for design 1.

Diffusion factor: A possible approach to the study of compressor blade-row performance would be to treat the axial-velocity ratio $V_{z,2}/V_{z,1}$ as a blade loading parameter peculiar to the three-dimensional flow problem and attempt to correlate its effects with those of parameters common to three-dimensional and two-dimensional flow: solidity, relative inlet flow angle, and turning angle. A diffusion factor D has been developed which is a function of the foregoing variables and which was derived to give an indication of the local blade suction-surface pressure gradient. This parameter has served to correlate loss data for several cases of both two-dimensional and three-dimensional flow (ref. 11).

The diffusion factor D is calculated as follows:

$$D = 1 - \frac{V_2'}{V_1'} + \frac{\Delta V_\theta'}{2\sigma V_1} \tag{7}$$

In terms of the axial-velocity ratio, relative flow angles, and solidity,

$$D = 1 - \frac{V_{z,2}}{V_{z,1}} \cos \beta_1' \left(\sec \beta_2' + \frac{\tan \beta_2'}{2\sigma} \right) + \frac{\sin \beta_1'}{2\sigma} \tag{8}$$

Values of rotor D factor for designs 1 and 4 are plotted against angle of attack in figure 16.

For each design at a given radius, the D factors calculated for the various speeds, for which the data are available, correlate into essentially a single curve. It would be reasonable to expect an increase in D factor with Mach number because of the compressibility effect on the axial-velocity ratio. A slight trend of this sort is indicated, but the magnitude of the effect does not appear to be significant.

Discussion of rotor D factors: A comparison of rotor D factors for designs 1 and 4 is presented in figure 17. The curves as drawn through the data points in figure 16 are reproduced in figure 17 along with D factors calculated from the cascade-predicted turning angles. Three trends are revealed in figure 17 at a given angle of attack: (1) D factor is generally higher near the tip than near the hub for both designs; (2) D factor is appreciably higher for design 1 than for design 4 (except near the hub where there is little difference between the two designs); and (3) near the tip, D factor for design 1 is appreciably larger than cascade-predicted D, whereas, for design 4, the compressor and cascade-predicted D agree quite well at all radii.

The values of D factor calculated from compressor performance can differ from cascade-predicted D factor (for a given relative-inlet-flow angle) only if the compressor turning angles differ from cascade-predicted turning angles, or if the axial-velocity ratio $V_{z,2}/V_{z,1}$ is different from unity. In the case of design 1, the compressor turning angles near the tip are less than the cascade-predicted values (fig. 13). In itself, this trend would operate to lower the rate of diffusion. (From formula (8), increased β_2' for a given β_1' would decrease the value of D factor.) However, the axial-velocity ratio $V_{z,2}/V_{z,1}$ near the tip is considerably less than unity (fig. 9), and the tendency of low axial-velocity ratio to increase the diffusion rate has the decisive effect on the final value of D factor. In the case of design 4, turning angles and axial-velocity ratios both agree fairly well with the cascade-predicted values; therefore, the D factors naturally agree.

Comparison of rotor turning angles with D factor: A comparison of the design 1 tip-region turning angle and D factor characteristics (figs. 13 and 17) reveals that at station a where the turning-angle curves for design 1 peak at relatively low angles of attack, the D factors are considerably higher than those predicted by cascade data. A tentative interpretation can be drawn from this comparison that the blade loading is high enough even at relatively low angles of attack for flow separation to occur with a consequent decrease in the turning angle.

The preceding discussion supplies a qualitative explanation for the tip-region turning-angle characteristics of design 1. A quantitative correlation of turning with D factor is obviously desirable, but turning angle is not a convenient parameter with which to attempt such a correlation. Comparisons are therefore made between D factor and the deviation angle. The fact that deviation angle varies only slightly with angle of attack (in the good flow range) should facilitate a quantitative correlation. In order to employ deviation angles, the camber angle of a circular-arc blade section equivalent to the 65-(12)10 blade section must first be computed. It is assumed, for this purpose, that if the circular-arc and 65-series camber lines have the same maximum height as a percentage of chord length, the two blade sections are equivalent. On this basis, the circular-arc blade section equivalent to a 65-(12)10 blade section has a camber angle φ of 30.1°.

Comparison of rotor deviation angles with D factor: A comparison of the rotor deviation angles Δ and the cascade-predicted deviation angles for designs 1 and 4 is presented in figure 18 plotted against D factor. At each radial station, the cascade data for designs 1 and 4 can be represented by a single curve with a maximum discrepancy of ±1°. As D factor exceeds about 0.5, the cascade-predicted deviation angles increase rapidly.

The compressor data extend appreciably into the high-D-factor range ($D > 0.5$) only at station a. The correlation of the rotor deviation angles with the cascade-predicted deviation angles actually appears to be best within this high-D-factor range except for very high D factors ($D > 1$). In the range of D factor up to 0.5, the rotor deviation angles for design 4 are lower than the cascade-predicted values at stations a and c, whereas for design 1 the rotor deviation angles are higher than the cascade-predicted values at station e. These discrepancies in the low-D-factor range cannot be entirely accounted for; they are probably due to a combination of experimental error and three-dimensional flow effects which cannot be evaluated from the data.

It is suggested that the main value of the deviation angle - D factor correlation lies in its possible use in a cascade-data correction method for the high-D-factor range.

Comparison of rotor loss with D factor: A comparison of the rotor losses (fig. 15) with the rotor D factors (fig. 17) shows that high diffusion rates (indicated by high D factors) are accompanied by high losses. At the tip region, the D factors for design 1 are not only much larger than for design 4; they are also much larger than the cascade-predicted values for design 1. In contrast, the measured and cascade-predicted D factors for design 4 agree very well. It should not be

expected from this comparison that the measured rotor losses and cascade-predicted losses for design 4 should agree at this tip region. The cascade-predicted loss is essentially a profile-loss, whereas the measured rotor loss also includes other increments of loss peculiar to three-dimensional flow. These include losses caused by secondary flows associated with the casing boundary layer and tip clearance. Also, in the case of a rotor, it is possible to measure at the tip region some of the losses incurred at blade elements near the hub. The investigations of reference 13 indicated that some of the low-energy air at the blade-surface boundary layer would travel radially when it reached the blade wake. In the case of a rotor, this radial motion would be towards the tip. For these reasons the minimum possible tip-region losses probably exceed appreciably the corresponding cascade-predicted losses.

A quantitative comparison of rotor losses and diffusion characteristics is presented in figure 19, where the measured rotor losses $\bar{\omega}$ for designs 1 and 4 are plotted against rotor D factor for the three radial stations. Also plotted are the corresponding cascade-predicted loss parameters. The feature of primary interest in figure 19 is the fact that a limited region of correlation between designs 1 and 4 of loss against D factor (shown by the dashed line) is indicated by the available data at station a. As D factor exceeds 0.55, the losses at this tip region increase rapidly, and the data for both designs plot approximately on the same curve. In contrast, the data at low D factors differ greatly in the values of loss for the two designs, which indicates that, at angles of attack less than the angle of attack for minimum loss, the D factor cannot be used to estimate losses. This trend can be explained as follows: As discussed in reference 11, the D factor was derived in order to provide an indication of the blade suction-surface pressure gradient for operation in the low-loss region. The assumptions on which the derivation of the D factor was based are not fulfilled by the flow conditions at angles of attack other than the angle of attack for minimum loss. As angle of attack decreases from the minimum-loss value, the calculated D factors decrease, but losses increase. At high angles of attack, however, the D factors and losses are both high, and an approximate correlation is obtained for tip-region rotor losses.

The minimum-loss tip-region values of $\bar{\omega}$ and D factor for design 1 were approximately 0.150 and 0.60, respectively; and for design 4, the corresponding values were 0.065 and 0.40. These results correlate well with the data presented in figure 8 of reference 11 and illustrate the importance of designing for low D factor at the tip region in order to minimize losses. At stations c and e, the data did not extend into the range of high D factors.

Stator blade-element performance. - The available stator blade-element performance data were obtained from the full-stage investigations of designs 3 and 4. As discussed in the section Instrumentation, no measurements were made between the rotor and stator blade rows for the full-stage investigations of designs 1 and 2; hence, their stator performance is not available. The stator inlet Mach numbers are plotted

against stator angle of attack α_2 in figure 20, so that the possibility of Mach number effects on loss can be analyzed. For design 3, the highest stator inlet Mach number slightly exceeded 0.90, and for design 4, the highest Mach number was about 0.78.

The stator performance for designs 3 and 4 is presented in terms of turning angle ϵ_2 and stator losses $\bar{\omega}$ plotted against stator angle of attack α_2.

Turning angles: Stator turning angles ϵ_2 are plotted against angle of attack α_2 in figure 21 for designs 3 and 4. For design 3, the variation of turning angle with angle of attack is very nearly linear, even at the tip-region measuring station. The slopes of all the curves lie within the range from 0.75 to 0.83.

Because of the invalid measurements of flow angles at 120 and 135 percent design speed (discussed in the section Experimental procedure), the turning angles for these speeds are not presented.

Comparisons of stator turning angles with cascade data: The curves drawn through the data points of figure 21 are reproduced in figure 22 for comparison with the corresponding cascade data. Because of the similarity of the velocity diagrams of designs 3 and 4 (fig. 7), the cascade-predicted turning angles for the two designs are practically the same. The slopes of the measured turning-angle curves and the predicted curves agree very well. At the hub and mean radius, the design 3 turning angles check the cascade data within 2° except for low angles of attack at the mean radius; however, the design 4 data appreciably exceed the cascade-predicted values. At the tip, the measured turning angles for both designs are from 4° to 5° higher than the cascade data.

The general trend of the compressor turning angles to exceed the cascade-predicted values might be caused partly by a lower level of blade loading for the compressor stators than for the two-dimensional cascade. D factors were calculated for the cascade design points at station a ($\alpha_2 = 9.3^\circ$ for design 3, $\alpha_2 = 9.4^\circ$ for design 4). For both sets of stators, the D factors were about 0.32; for the design 3 and design 4 cascade data, the D factors were 0.40 and 0.35, respectively. Thus, part of the high turning for the stators is probably due to this lower level of loading, and part is due to experimental error. (Plots of stator D factors are not presented because of the small range of D factor covered by the stator operation.)

Total-pressure losses: The stator total-pressure-loss parameter $\bar{\omega}_2$ for designs 3 and 4 is plotted against stator angle of attack α_2 in figure 23. (The design 3 loss parameters for 120 and 135 percent design speeds are included because the invalid angle measurements do not affect the values of $\bar{\omega}$.)

[redacted]

No essential difference in the loss characteristics of the two designs is indicated for the speeds up to design speed. Both sets of curves show a wide range of angle of attack at low loss, and little variation in loss is indicated from tip to hub. An interesting comparison can be made with the guide-vane losses. For the guide vanes, the minimum values of $\overline{\omega}$ are about 0.060 (from the mean radius to the hub); whereas, for the stators, a typical value of $\overline{\omega}$ is about 0.040. This result indicates that the stators, with their 65-(12)10 blade section, perform with less loss in a flow with an adverse pressure gradient than do the sheet metal guide vanes in a flow with a favorable pressure gradient. This trend is probably caused partly by the higher frictional drag of a flat plate compared to the profile drag of an airfoil section of the same chord (p. 124, ref. 13) and partly by the higher frictional drag resulting from the higher solidities and larger chords of the guide vanes near the tip (fig. 1).

No well-defined Mach number effect on loss is exhibited for design 4. None would be expected in view of the fact that the Mach number range for the highest speed investigated (115 percent design speed) was 0.60 to 0.75 (fig. 20). For design 3, however, a marked increase in loss is observed for the investigations at 120 and 135 percent design speed. The Mach number ranges were, respectively, 0.63-0.83 and 0.70-0.92.

Discussion of stator losses: The curves drawn through the data points of figure 23 are reproduced in figure 24 for comparison with the cascade-predicted values of $\overline{\omega}$.

The cascade-predicted losses are almost identical for both sets of stators because their inlet air angles differ by only a few degrees at any given angle of attack (by 5.6° at station a and 1.3° at station e).

The minimum stator-blade losses appreciably exceed the cascade-predicted values. This trend is similar to that which was observed for rotor-blade losses, namely, that the blade-profile losses are only part of the loss incurred across a compressor blade row.

Comparisons of stator turning and loss with D factor are not made, because the available stator data did not extend into the high-D-factor range except during rotor-stall conditions which resulted in very high stator angles of attack.

The available data indicate that for designs similar to designs 3 and 4, the prediction of stator loss is not a difficult problem, and that the level of stator loss is quite low for a wide range of angle of attack. Figure 24 shows that the minimum value of $\overline{\omega}$ lies within the range from approximately 0.025 to approximately 0.050 for both designs and at all measuring stations.

The high losses for designs 3 that were obtained at 120 and 135 percent design speeds (fig. 23) are probably caused mostly by local blade-surface shock phenomena. The inlet Mach numbers at these speeds ranged from approximately 0.70 to 0.90 (fig. 20). The investigation of reference 15 showed, in the case of an annular cascade utilizing the 65-(12)10 blade, that inlet Mach numbers of 0.80 were accompanied by local blade-surface peak Mach numbers of 1.30. The shock-diffusion of these velocities to subsonic values was accompanied by high losses, partly due to shock loss and also to aggravated flow separation from the blade surface.

Part of this loss for design 3 could be a consequence of increased diffusion caused by the compressibility effect of high Mach number on the axial-velocity ratio. However, this cannot be proved because the flow-angle data for the 120 and 135 percent design speeds, upon which the calculation of D factor depend, are believed to be invalid.

Discussion of efficiency and range characteristics. - The rotor blade-element loss data for designs 1 and 4 discussed in the preceding paragraphs provide a basis for an analysis of the trends of increasing over-all efficiency and flow-coefficient range as design axial-velocity ratio $(V_z/U_t)_h$ is increased.

The analysis of blade-element turning-angle and loss data showed that the main differences in performance occurred in the rotor-tip region. The study of the efficiency and range characteristics presented in the section Over-All Performance can therefore be reduced to a study of the tip-region blade-element efficiency and range characteristics. The full-stage investigations provided the only data which can be directly compared among all four designs; therefore, tip-region stage-element efficiencies are presented in figure 25.

Tip-region stage-element efficiencies: Stage-element efficiency is defined as the ratio of the ideal stagnation enthalpy rise between the measuring stations upstream of the rotor and downstream of the stator to the actual enthalpy rise. The efficiencies obtained from the design-speed investigations of the four designs were plotted against radius after stator r_3 for each operating point; the values of efficiency for each design at the same radius, $r_3 = 0.522$ foot (station a for design 4), were then plotted against angle of attack. These tip-region efficiency characteristics are presented in figure 25.

Figure 25 shows that the peak stage-element efficiencies for designs 2, 3, and 4 are markedly higher than the peak efficiency for design 1. Also, a definite increase in range of angle of attack at a given efficiency is indicated for the successive designs. For instance, an efficiency η_{se} of at least 0.80 is indicated for the ranges of angle of attack summarized in the following table. (Also included are the peak efficiencies.)

Design number	Peak η_{se}	Range of α at $\eta_{se} \geq 0.80$, deg
1	0.85	7.6
2	.90	12.4
3	.885	15.2
4	.90	15.8

The increase in peak efficiency between design 1 and the other three designs is caused by the more favorable rotor diffusion characteristics of these high-axial-velocity designs with their consequently decreased rotor blade-element losses. Also, these lower diffusion rates for the high-axial-velocity designs permit operation at increased angles of attack before critical values of D factor are reached; therefore, the low-loss range of angle of attack is greater for the high-axial-velocity designs. A wide angle-of-attack range at low loss is reflected, of course, in a wide angle-of-attack range at high efficiency.

Discussion of increased range: In the section Dimensionless over-all performance the ranges of flow coefficient for an over-all efficiency of at least 0.80 were compared. It was shown that the flow-coefficient range increased as design axial-velocity ratio $(V_z/U_t)_h$ increased.

The over-all range of flow coefficient is a combination of the average blade-element angle-of-attack range and the average change of angle of attack for a given change in flow coefficient. It is necessary to analyze these two characteristics only at the tip region, because the over-all range is limited by the tip-region performance. It has been shown in the previous section that the tip-region angle-of-attack range for design 1 is limited by high rates of diffusion of relative velocity. The change of angle of attack for a given change in flow coefficient is presented next.

Rotor angle of attack at station a is plotted against the flow coefficient $(V_z/U_t)_{av}$ for the four designs in figure 26. The following table summarizes values of the change in flow coefficient that would be required for a 10° change in angle of attack.

Design number	Change of flow coefficient
1	0.095
2	.130
3	.145
4	.170

The flow-coefficient range for design 1 is thus limited both by a narrow range of angle of attack for a given efficiency and by the fact that for a given change in angle of attack, the change in flow coefficient is least for design 1.

The rapid rate of change of angle of attack with flow coefficient for design 1 is a direct consequence of the velocity-diagram geometry. In reference 8, it was shown that the rate of change of angle of attack with the axial-velocity ratio $V_{z,1}/U_t$ is given by the following formula:

$$\frac{d\alpha}{d\left(\frac{V_{z,1}}{U_t}\right)} = -\frac{r_t}{r}\left(\sin\beta_1' + \cos\beta_1' \tan\beta_1\right)^2$$

It must be emphasized that the axial-velocity ratio $V_{z,1}/U_t$ is the local value at a given radius; it is not the same as the flow coefficient $(V_{z,1}/U_t)_{av}$, and in general,

$$\frac{d\left(\frac{V_{z,1}}{U_t}\right)}{d\left(\frac{V_{z,1}}{U_t}\right)_{av}} \neq 1$$

The following table summarizes values of $\left|\frac{d\alpha}{d\left(\frac{V_z}{U_t}\right)}\right|$ calculated from the design velocity diagrams for the four compressors at a radius ratio of 0.95, and values of $\left|\frac{d\alpha}{d\left(\frac{V_z}{U_t}\right)_{av}}\right|$ measured from figure 26.

[redacted]

(The angle α is expressed in radians.)

Design number	$\left\lvert \frac{d\alpha}{d\left(\frac{V_{z,1}}{U_t}\right)} \right\rvert$	$\left\lvert \frac{d\alpha}{d\left(\frac{V_{z,1}}{U_t}\right)_{av}} \right\rvert$
1	2.31	1.87
2	1.68	1.31
3	1.29	1.13
4	1.03	.91

Thus, for design 1, both the high-D-factor effects on tip-region losses and the effects of the velocity-diagram geometry on the rate of change of angle of attack with flow coefficient tend to limit the tip-region range and therefore the over-all range of flow coefficient.

Radial Equilibrium Considerations

The assumption of symmetrical velocity diagram and constant stagnation enthalpy in the design causes, through the action of radial equilibrium, a large variation of axial velocity along the radius. Furthermore, this axial-velocity gradient is larger downstream of the rotor than upstream of the rotor. Since radial displacements of flow obviously exist, the validity of the simplified-radial-equilibrium equation cannot be taken for granted. The following paragraphs present results of two types of radial-velocity-distribution calculations which incorporate the assumption of simplified radial equilibrium.

The radial pressure gradient is given by the following equation (ref. 16):

$$\frac{1}{\rho}\frac{dp}{dr} = \frac{V_\theta^2}{r} - V_r\frac{\partial V_r}{\partial r} - V_z\frac{\partial V_r}{\partial z} \tag{9}$$

Also, from the combined and first and second laws of thermodynamics and the steady-flow energy equation,

$$\frac{1}{\rho}\frac{dp}{dr} = \frac{dH}{dr} - \frac{d}{dr}\left(\frac{V^2}{2}\right) - t\frac{dS}{dr} \tag{10}$$

[redacted]

Isentropic simplified radial equilibrium. - The equation used in the analysis of reference 1 and in the design calculations of the radial-velocity distribution upstream of the rotor and downstream of the stator was obtained by making the assumption that $\partial V_r/\partial r$, $\partial V_r/\partial z$, and dS/dr were all negligible. Then equation (9) becomes

$$\frac{1}{\rho}\frac{dp}{dr} = \frac{V_\theta^2}{r} \text{ (simplified radial equilibrium)} \qquad (9a)$$

and equation (10) becomes

$$\frac{1}{\rho}\frac{dp}{dr} = \frac{dH}{dr} - \frac{d}{dr}\left(\frac{V^2}{2}\right) \qquad (10a)$$

Calculations were made at the three axial measuring stations for the available data of the four designs to check the validity of these design assumptions. The velocity distributions were calculated which, for the measured temperature rise and absolute flow-angle distribution, would satisfy equations (9a) and (10a), and the continuity condition. The results in terms of the axial-velocity ratio V_z/U_t plotted against radius ratio r/r_t are presented in figure 27.

The calculated axial-velocity ratios for the axial station upstream of the rotor (fig. 27) check the measured values quite well except near the tip for some of the low-flow runs. Also, this correlation is fairly good downstream of the rotor (figs. 27(a) and (d)). However, an appreciable discrepancy exists between the calculated axial-velocity ratios and the measured values downstream of the stators, especially near the tip (fig. 27). The question arises whether this discrepancy was caused primarily by the assumption that the radial acceleration terms of equation (9) are negligible, or by the assumption that the entropy gradient term of equation (10) is negligible. A logical approach would be to include the effect of the entropy gradient because (1) the main difference between conditions upstream of the rotor and downstream of the stator (aside from the level of enthalpy) is the radial variation of blade losses, and (2) the entropy gradient can be evaluated from measured stagnation values of pressure and temperature.

Nonisentropic simplified radial equilibrium. - For the axial stations downstream of the rotor and stator, velocity distributions were calculated which satisfy equations (9a) and (10), and the condition of continuity. The results, in terms of the axial-velocity ratio V_z/U_t plotted against radius ratio r/r_t, are shown in figure 27 for comparison with the isentropic-simplified-radial-equilibrium calculation.

The calculated axial-velocity ratios after rotor (figs. 27(a) and (d)) are slightly lower near the tip and higher near the hub than the isentropic values. The results of the two calculations are not greatly different, but near the tip, the nonisentropic calculation checks the data better than does the isentropic calculation.

The main effect of the entropy gradient occurs after the stator (fig. 27). The nonisentropic calculation checks the data very well except near the hub, where the calculated values of axial-velocity ratio are lower than the measured values.

Probably this small discrepancy is a consequence of neglecting the radial acceleration terms of equation (4); these terms would probably be most significant near the hub because of the influence of the hub curvature.

SUMMARY OF RESULTS

The analysis of the over-all performance and blade-element performance of four axial-flow single-stage compressors designed for constant stagnation enthalpy radially and symmetrical velocity diagrams at all radii and having a hub-tip radius ratio of 0.5 gave the following results:

1. For a given Mach number limit, high pressure ratio required a design assumption of low specific weight flow (low design axial-velocity ratio $(V_z/U_t)_h$). Because of the action of radial equilibrium, this design assumption resulted in high rotor-tip-region rates of diffusion (as measured by the D factor) with consequent high losses and low peak efficiencies. Therefore the most suitable use for the symmetrical-velocity-diagram was for lower pressure ratio and higher specific weight flow designs.

2. For the available rotor blade-element data, a correlation for a given solidity was obtained among compressor and cascade-predicted deviation angles as functions of D factor.

3. For the low-D-factor design (design 4) fairly good correlation was obtained between cascade-predicted and rotor turning angles as functions of angles of attack.

4. A correlation of tip-region rotor relative-total-pressure losses for designs 1 and 4 as functions of D factor was obtained for D factors exceeding approximately 0.55. The cascade-predicted losses did not correlate with tip-region rotor losses because the latter are influenced by other factors in addition to blade-suction-surface flow separation.

5. The over-all range of flow coefficient (or weight flow) for the lowest-axial-velocity design at a given value of efficiency was limited by the high tip-region total-pressure losses caused by high D factors and the high rate of change of angle of attack with flow coefficient imposed by high guide-vane turning.

6. The available stator data represented the low-D-factor type of design. The stator blade-element minimum losses varied only slightly with radius and between the two designs for which data were available.

7. The available data indicated that the assumption of simplified radial equilibrium was a valid one. For most of the cases investigated, the axial-velocity profiles obtained from the calculation neglecting entropy gradient agreed fairly well with the data at the rotor inlet and outlet. In order to obtain good agreement between the calculated axial velocities and the data downstream of the stators, it was necessary to include the effect of the entropy gradient. A small discrepancy remained between the predicted and measured velocities near the hub, which was probably caused by the omission of the radial acceleration terms from the radial-equilibrium equation.

Lewis Flight Propulsion Laboratory
National Advisory Committee for Aeronautics
Cleveland, Ohio, November 9, 1953

[redacted]

APPENDIX A

SYMBOLS

The following symbols are used in this report:

A	annular area
a	velocity of sound
C_L	camber (lift coefficient of isolated airfoil)
D	diffusion parameter
H	stagnation enthalpy
K	constant in Kantrowitz-Daum equation
M	Mach number
P	stagnation pressure
p	static pressure
R	gas constant
r	radius
S	entropy
T	stagnation temperature
U	rotor wheel speed
V	absolute air velocity
W	weight flow
$W\sqrt{\theta}/\delta$	weight flow corrected to NACA standard sea-level pressure and temperature
α	angle of attack
α_0	angle of attack at zero lift
β	absolute air angle, angle between compressor axis and absolute air velocity

[redacted]

γ ratio of specific heats

Δ deviation angle, angle between relative air velocity and tangent to camber line at trailing edge

δ ratio of inlet stagnation pressure to NACA standard sea-level pressure

ϵ turning angle

η adiabatic temperature-rise efficiency

θ ratio of inlet stagnation temperature to NACA standard sea-level temperature

ξ blade-angle setting, angle between compressor axis and blade chord

ρ static density

σ solidity, ratio of chord length to distance between adjacent blades

φ camber angle, angle between tangents to camber line at leading and trailing edges

$\bar{\omega}$ relative total-pressure-loss parameter

Subscripts:

0 depression tank

1 upstream of rotor

2 downstream of rotor

3 downstream of stator

av average

des design value

e blade element

gv guide vane

h hub

id ideal

mr mean radius

r radial direction

se stage element

std standard

T stagnation condition

t tip

z axial direction

θ tangential direction

Superscript:

' relative to blade row

APPENDIX B

DERIVATION OF EQUATIONS AND METHODS OF CALCULATION

Design tip speed. - The formula for design tip speed (eq. (3)) is obtained as follows:

$$M_{1,h}'^2 = \frac{\left(\frac{V_1'}{U_t}\right)_h^2}{\left(\frac{a}{U_t}\right)_h^2} = \frac{\left(\frac{V_{z,1}}{U_t}\right)_h^2 + \left(\frac{U}{U_t} - \frac{V_{\theta,1}}{U_t}\right)_h^2}{(\gamma-1)\left[\frac{H_1}{U_t^2} - \frac{1}{2}\left(\frac{V_1}{U_t}\right)_h^2\right]}$$

$$= \frac{\left(\frac{V_{z,1}}{U_t}\right)_h^2 + \left(\frac{U}{U_t}\right)_h^2 - 2\left(\frac{UV_\theta}{U_t^2}\right)_h + \left(\frac{V_{\theta,1}}{U_t}\right)_h^2}{(\gamma-1)\left[\frac{H_1}{U_t^2} - \frac{1}{2}\left(\frac{V_1}{U_t}\right)_h^2\right]}$$

$$= \frac{\left(\frac{V_1}{U_t}\right)_h^2 + \frac{U_h}{U_t}\left(\frac{U}{U_t} - \frac{2V_{\theta,1}}{U_t}\right)_h}{(\gamma-1)\left[\frac{H_1}{U_t^2} - \frac{1}{2}\left(\frac{V_1}{U_t}\right)_h^2\right]}$$

By assumptions of symmetrical velocity diagram and constant enthalpy addition,

$$\frac{U_h}{U_t}\left(\frac{U}{U_t} - \frac{2V_{\theta,1}}{U_t}\right)_h = \frac{U_h}{U_t}\left(\frac{V_{\theta,1}'}{U_t} - \frac{V_{\theta,1}}{U_t}\right)_h = \frac{U_h}{U_t}\left(\frac{V_{\theta,2}}{U_t} - \frac{V_{\theta,1}}{U_t}\right)_h$$

$$= \frac{U_h}{U_t}\frac{\Delta V_{\theta,h}}{U_t}$$

$$= \frac{U\Delta V_\theta}{U_t^2}$$

$$\therefore \quad M'^{2}_{1,h} = \frac{\left(\frac{V_1}{U_t}\right)^2_h + \frac{U\Delta V_\theta}{U_t^2}}{(\gamma-1)\left[\frac{H_1}{U_t^2} - \frac{1}{2}\left(\frac{V_1}{U_t}\right)^2_h\right]}$$

Rearrangement yields equation (3):

$$\frac{H_1}{U_t^2} = \frac{\left(1 + \frac{\gamma-1}{2} M'^{2}_{1,h}\right)\left(\frac{V_1}{U_t}\right)^2_h + \frac{U\Delta V_\theta}{U_t^2}}{(\gamma-1)\, M'^{2}_{1,h}} \tag{3}$$

Design tip speed is then computed from the value of enthalpy for standard air.

Rating methods. - The average pressure ratio is based on the mass-averaged isentropic power input (ref. 17)

$$\left(\frac{P_3}{P_0}\right)_{av} = \left\{ \frac{\int_{r_{3,h}}^{r_t} \left[\left(\frac{P_3}{P_0}\right)^{\frac{\gamma-1}{\gamma}} - 1\right] \rho_3 V_{z,3} r_3 dr}{\int_{r_{3,h}}^{r_t} \rho_3 V_{z,3} r_3 dr} + 1 \right\}^{\frac{\gamma}{\gamma-1}} \tag{B1}$$

The pressure ratio is computed in the form of equation (B1) because the quantity $\left[\left(\frac{P_3}{P_0}\right)^{\frac{\gamma-1}{\gamma}} - 1\right]$ is a tabulated function of pressure ratio. In its simplest form, equation (B1) reduces to

$$\left(\frac{P_3}{P_0}\right)_{av} = \left\{ \frac{\int_{r_{3,h}}^{r_t} \left(\frac{P_3}{P_0}\right)^{\frac{\gamma-1}{\gamma}} \rho_3 V_{z,3} r_3 dr}{\int_{r_{3,h}}^{r_t} \rho_3 V_{z,3} r_3 dr} \right\}^{\frac{\gamma}{\gamma-1}} \tag{B1a}$$

The average adiabatic temperature-rise efficiency is based on the ratio of the mass-averaged isentropic power input to the mass-averaged actual power input (ref. 17).

$$\eta_{av} = \frac{\int_{r_{3,h}}^{r_t} T_0 \left[\left(\frac{P_3}{P_0} \right)^{\frac{\gamma-1}{\gamma}} - 1 \right] \rho_3 V_{z,3} r_3 dr}{\int_{r_{3,h}}^{r_t} \left[T_3 - T_0 \right] \rho_3 V_{z,3} r_3 dr} \tag{B2}$$

Calculations were made of η_{av} in the form of equation (B2) because the quantity $\left[\left(\frac{P_3}{P_0} \right)^{\frac{\gamma-1}{\gamma}} - 1 \right]$ is a tabulated function of pressure ratio, and the temperature rise $T_3 - T_0$ is a directly measured datum. Equation (B2) reduces to the following:

$$\eta_{av} = \frac{\left(\frac{P_3}{P_0} \right)_{av}^{\frac{\gamma-1}{\gamma}} - 1}{\left(\frac{T_3}{T_0} \right)_{av} - 1} \tag{B2a}$$

where $(P_3/P_0)_{av}$ is given by equation (1a) and

$$\left(\frac{T_3}{T_0} \right)_{av} = \frac{\int_{r_{3,h}}^{r_t} \frac{T_3}{T_0} \rho_3 V_{z,3} r_3 dr}{\int_{r_{3,h}}^{r_t} \rho_3 V_{z,3} r_3 dr}$$

The average ideal enthalpy addition is defined as the enthalpy rise corresponding to an isentropic process for the measured pressure ratio.

$$\left(\frac{\Delta H_{id}}{U_t^2} \right)_{av} = \frac{c_p T_0}{U_t^2} \left[\left(\frac{P_3}{P_0} \right)_{av}^{\frac{\gamma-1}{\gamma}} - 1 \right]$$

[redacted]

The flow coefficient is computed as follows:

$$\left(\frac{V_{z,1}}{U_t}\right)_{av} = \frac{\frac{W}{\rho_{1,av}A_1}}{U_t} = \frac{W}{\rho_T A_1 U_t \frac{\rho_{1,av}}{\rho_{1,T}}}$$

$$= \frac{W}{\rho_{std} A_1 U_t \frac{\rho_{1,av}}{\rho_{1,T}} \frac{\rho_T}{\rho_{std}}}$$

$$= \frac{W}{\rho_{std} A_1 U_t \frac{\rho_{1,av}}{\rho_{1,T}} \frac{P_1/T_1}{P_{std}/T_{std}}} = \frac{W \frac{T_1/T_{std}}{P_1/P_{std}}}{\rho_{std} A_1 U_t \frac{\rho_{1,av}}{\rho_{1,T}}}$$

$$\left(\frac{V_{z,1}}{U_t}\right)_{av} = \frac{W\sqrt{\theta}/\delta}{\rho_{std} A_1 U_t/\sqrt{\theta}} \left(\frac{\rho_{1,T}}{\rho_1}\right)_{mr} \tag{B3}$$

The assumption is made that the average static density upstream of the rotor equals the static density at the mean radius.

REFERENCES

1. Sinnette, John T., Jr.: Analysis of Effect of Basic Design Variables on Subsonic Axial-Flow-Compressor Performance. NACA Rep. 901, 1948. (Supersedes NACA RM E7D28.)

2. Burtt, Jack R.: Investigation of Performance of Typical Inlet Stage of Multistage Axial-Flow Compressor. NACA RM E9E13, 1949.

3. Burtt, Jack R., and Jackson, Robert J.: Performance of Single-Stage Compressor Designed on Basis of Constant Total Enthalpy with Symmetrical Velocity Diagram at all Radii and Velocity Ratio of 0.7 at Rotor Hub. NACA RM E51F06, 1951.

4. Sinnette, John T., Jr., Schey, Oscar W., and King, J. Austin: Performance of NACA Eight-Stage Axial-Flow Compressor Designed on the Basis of Airfoil Theory. NACA Rep. 758, 1943. (Supersedes NACA WR E-1.)

5. Johnsen, Irving A.: Investigation of a 10-Stage Subsonic Axial-Flow Research Compressor. I - Aerodynamic Design. NACA RM E52B18, 1952.

6. Kantrowitz, Arthur, and Daum, Fred L.: Preliminary Experimental Investigation of Airfoils in Cascade. NACA WR L-231, 1942. (Supersedes NACA CB.)

7. Abbott, Ira H., Von Doenhoff, Alfred E., and Stivers, Lewis S., Jr.: Summary of Airfoil Data. NACA WR L-560, 1945. (Supersedes NACA ACR L5C05.)

8. Jackson, Robert J.: Effects on the Weight-Flow Range and Efficiency of a Typical Axial-Flow Compressor Inlet Stage that Result from the Use of Decreased Blade Camber or Decreased Guide-Vane Turning. NACA RM E52G02, 1952.

9. Huppert, Merle C., Johnson, Donald F., and Costilow, Eleanor L.: Preliminary Investigation of Compressor Blade Vibration Excited by Rotating Stall. NACA RM E52J15, 1952.

10. Lieblein, Seymour, Lewis, George W., Jr., and Sandercock, Donald M.: Experimental Investigation of an Axial-Flow Compressor Inlet Stage Operating at Transonic Relative Inlet Mach Numbers. I - Over-All Performance of Stage with Transonic Rotor and Subsonic Stators up to Rotor Relative Inlet Mach number of 1.1. NACA RM E52A24, 1952.

11. Lieblein, Seymour, Schwenk, Francis C., and Broderick, Robert L.: Diffusion Factor for Estimating Losses and Limiting Blade Loadings in Axial-Flow Compressor Blade Elements. NACA RM E53D01, 1953.

12. Herrig, L. Joseph, Emery, James C., and Erwin, John R.: Systematic Two-Dimensional Cascade Tests of NACA 65-Series Compressor Blades at Low Speeds. NACA RM L51G31, 1951.

13. Rohlik, Harold, Allen, Hubert W., and Herzig, Howard: Study of Secondary-Flow Patterns in an Annular Cascade of Turbine Nozzle Blades with Vortex Design. NACA TN 2909, 1953.

14. Glauert, H.: The Elements of Aerofoil and Airscrew Theory. Second ed., Cambridge Univ. Press, 1948.

15. Briggs, William B.: Effect of Mach Number on the Flow and Application of Compressibility Corrections in a Two-Dimensional Subsonic-Transonic Compressor Cascade Having Varied Porous-Wall Suction at the Blade Tips. NACA TN 2649, 1952.

[redacted]

16. Wu, Chung-Hua, and Wolfenstein, Lincoln: Application of Radial-Equilibrium Condition to Axial-Flow Compressor and Turbine Design. NACA Rep. 955, 1950. (Supersedes NACA TN 1795.)

17. Mankuta, Harry, and Guentert, Donald C.: Investigation of Performance of Single-Stage Axial-Flow Compressor Using NACA 5509-34 Blade Section. NACA RM E8F30, 1948.

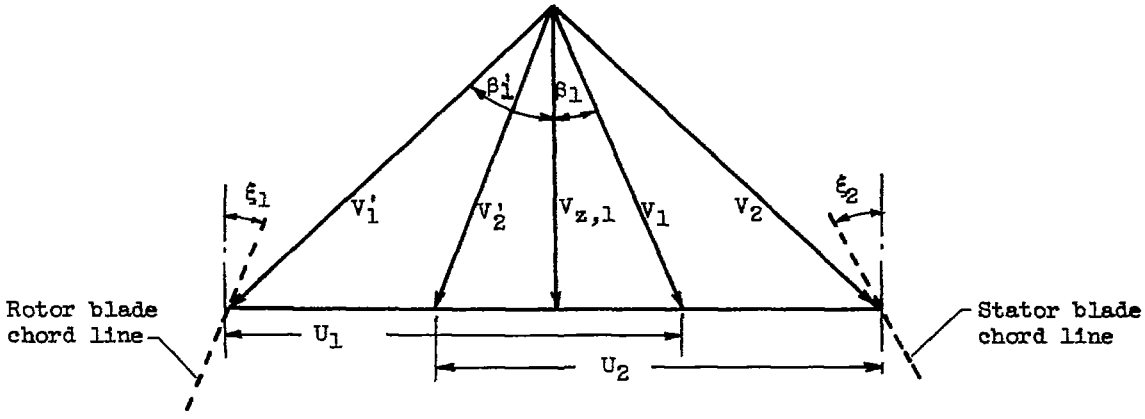

Typical velocity diagram

Design	r/r_t	$\frac{V_{z,1}}{U_t}$	φ_{gv}	β_1, deg	β_1', deg	ξ_1, deg	ξ_2, deg	σ_{gv}	σ_1	σ_2
	0.500	0.600	24.70	11.77	32.01	20.00		1.829	1.130	
	.541						22.00			1.102
	.600	.573	31.90	18.87	35.23	30.90	26.00	1.955	.942	.991
1	.700	.531	39.30	26.13	39.60	40.20	32.90	2.051	.807	.850
	.800	.473	47.45	34.22	45.31	48.30	40.60	2.150	.708	.745
	.900	.392	57.15	44.15	52.97	56.00	51.90	2.270	.628	.661
	1.000	.268	71.50	58.52	64.54	63.00	61.50	2.496	.565	.595
	0.500	0.700	16.63	8.63	29.35	14.80		1.240	1.130	
	.535						18.00			1.115
	.600	.679	22.88	14.88	31.70	21.50	21.80	1.406	.942	.991
2	.700	.647	28.95	20.95	31.98	28.00	27.70	1.522	.807	.850
	.800	.602	35.28	27.28	39.12	34.60	33.90	1.613	.708	.745
	.900	.542	42.33	34.33	44.32	41.20	40.40	1.711	.628	.661
	1.000	.463	50.78	42.78	51.01	47.80	46.90	1.831	.565	.595
	0.500	0.800	14.80	6.33	27.21	12.50		1.099	1.130	
	.530						15.10			1.125
	.600	.784	19.90	11.92	29.00	18.20	18.80	1.230	.942	.991
3	.700	.758	25.20	17.21	31.55	23.90	24.00	1.330	.807	.850
	.800	.722	30.50	22.51	34.76	29.60	29.20	1.404	.708	.745
	.900	.675	36.10	28.11	38.66	35.30	34.40	1.470	.628	.661
	1.000	.614	42.30	34.33	43.41	41.10	39.60	1.541	.565	.595
	0.500	0.900	13.00	4.45	25.54	10.80		0.966	1.130	
	.528						12.90			1.130
	.600	.888	17.68	9.77	27.32	16.30	16.30	1.095	.942	.991
4	.700	.866	22.34	14.35	28.91	21.20	20.90	1.183	.807	.850
	.800	.836	27.00	18.98	31.49	26.00	25.50	1.246	.708	.745
	.900	.797	31.70	23.71	34.59	30.80	30.10	1.296	.628	.661
	1.000	.748	36.40	28.73	38.26	35.40	34.80	1.333	.565	.595

Figure 1. - Design details of four axial-flow compressors having a hub-tip radius ratio of 0.5.

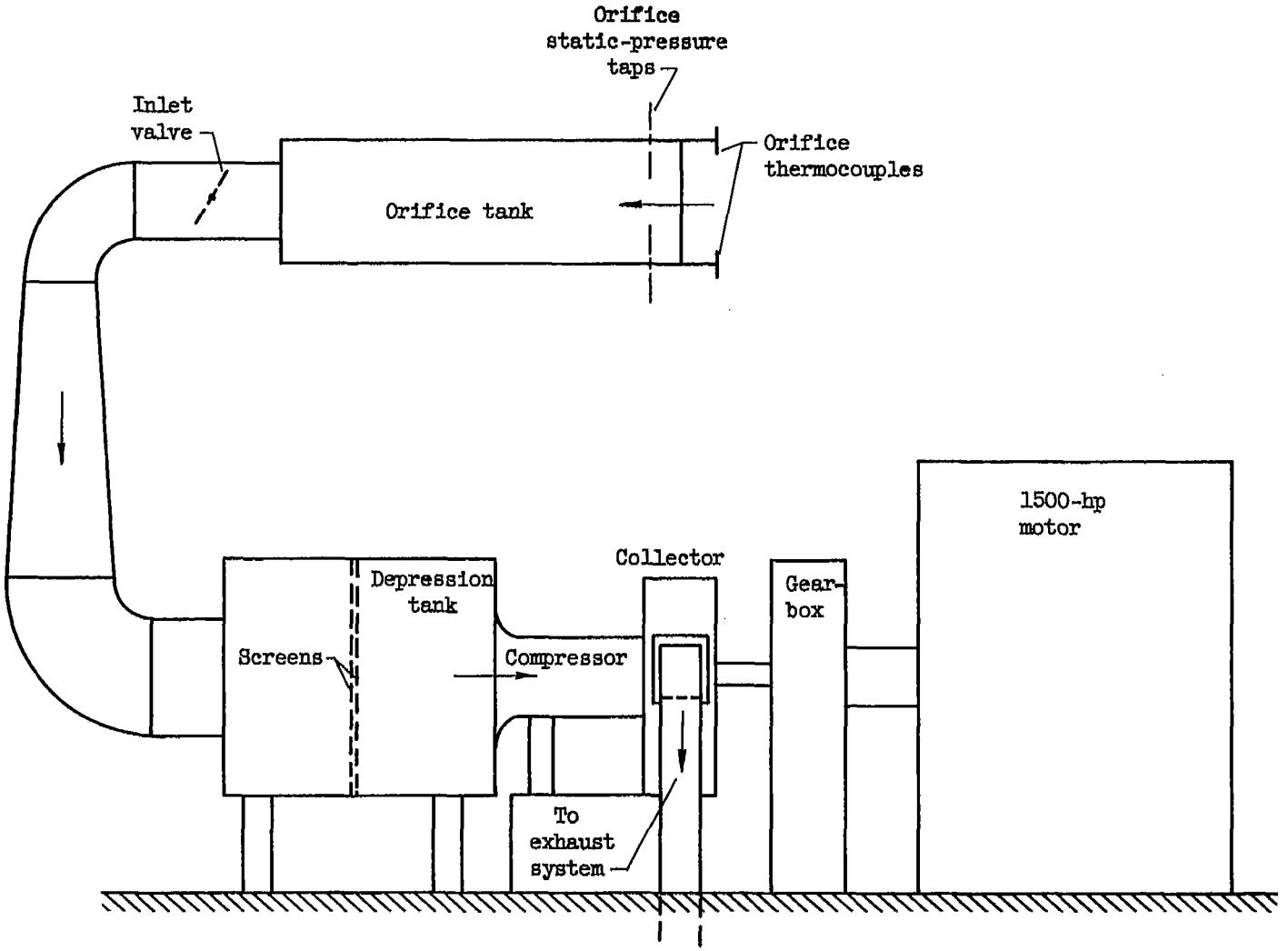

Figure 2. - Experimental setup.

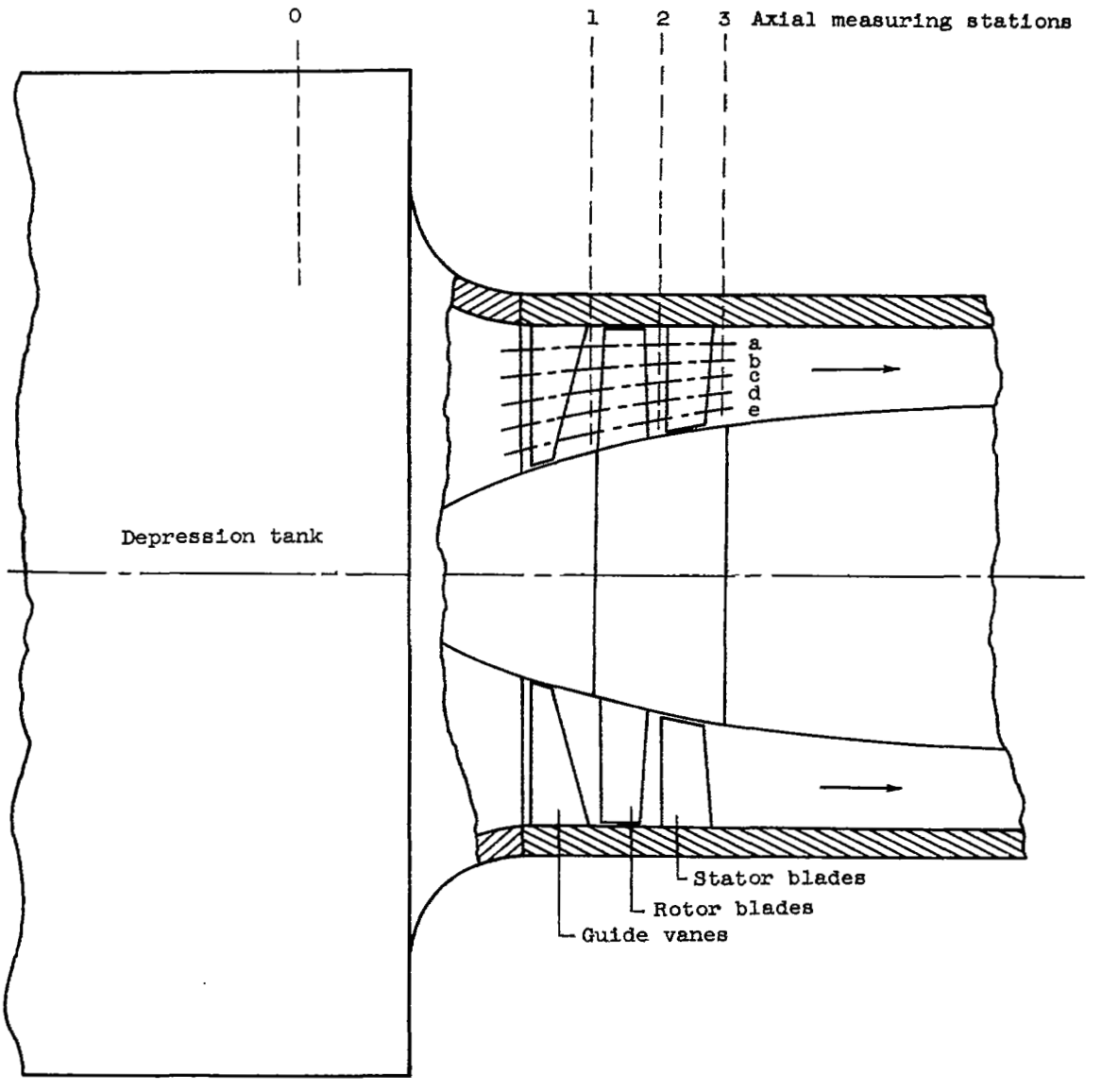

Figure 3. - Sketch showing instrumentation stations.

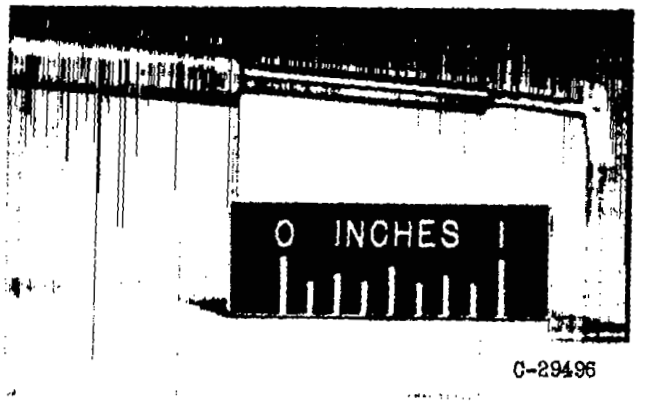

(a) Wedge-type static-pressure probe.

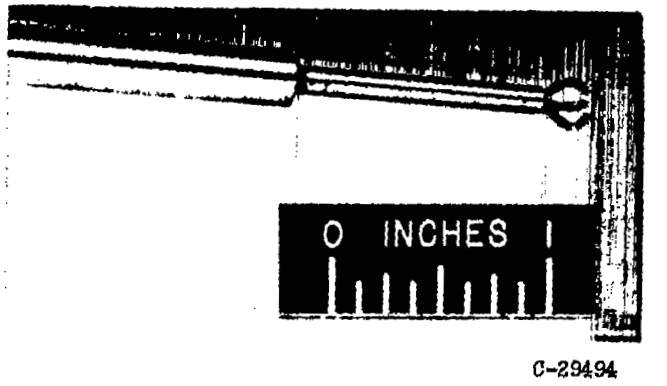

(b) Claw total-pressure-type yaw-measuring probe.

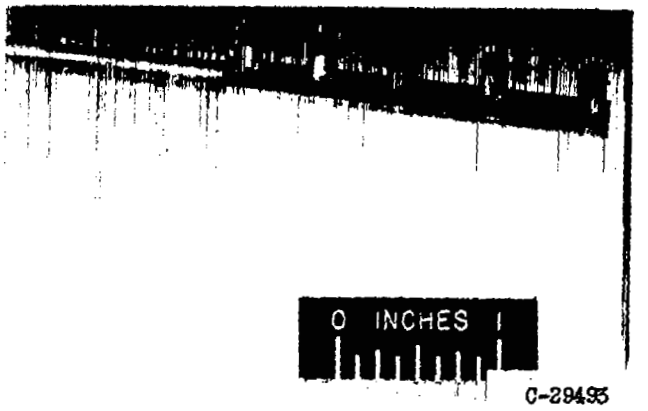

(c) Five-tip double-stagnation-type stagnation - temperature rake.

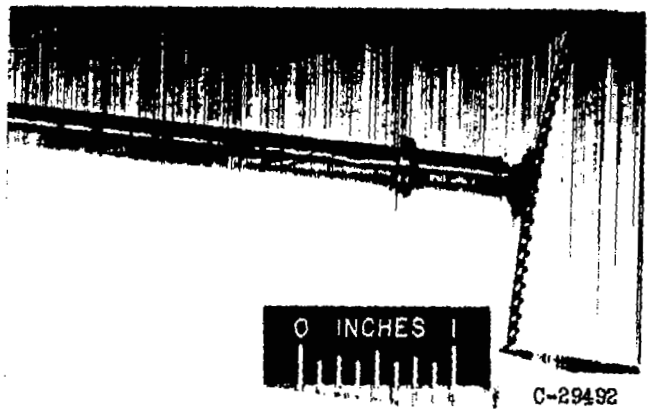

(d) Stagnation-pressure rake.

Figure 4. - Instrument probes.

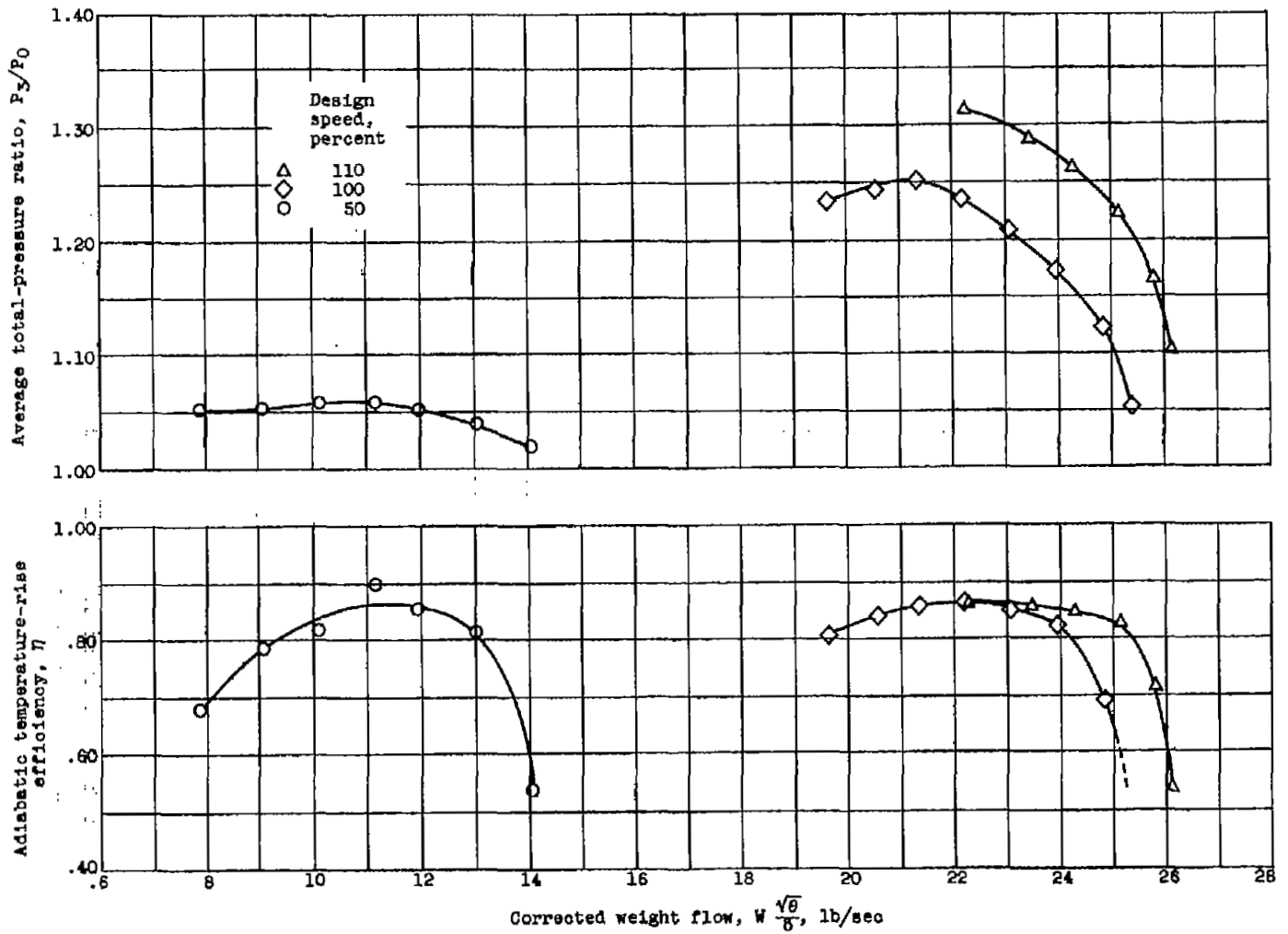

(a) Design 1; design corrected tip speed, $U_t/\sqrt{\theta}$, 1104 feet per second.

Figure 8. - Over-all performance of four axial-flow compressors having a hub-tip radius ratio of 0.5. Full-stage investigation.

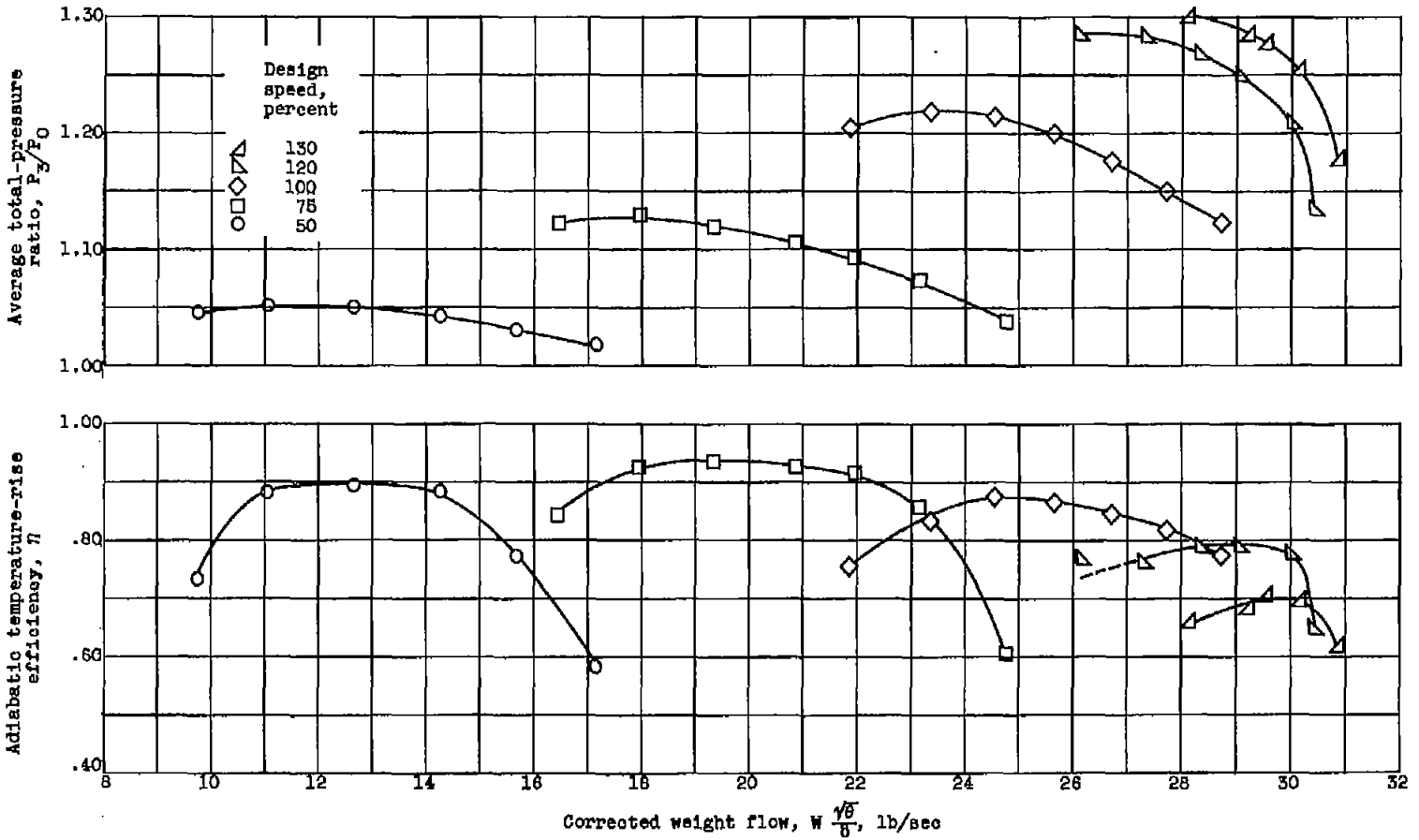

(b) Design 2; design corrected tip speed, $U_t/\sqrt{\theta}$, 938 feet per second.

Figure 5. - Continued. Over-all performance of four axial-flow compressors having a hub-tip radius ratio of 0.5. Full-stage investigation.

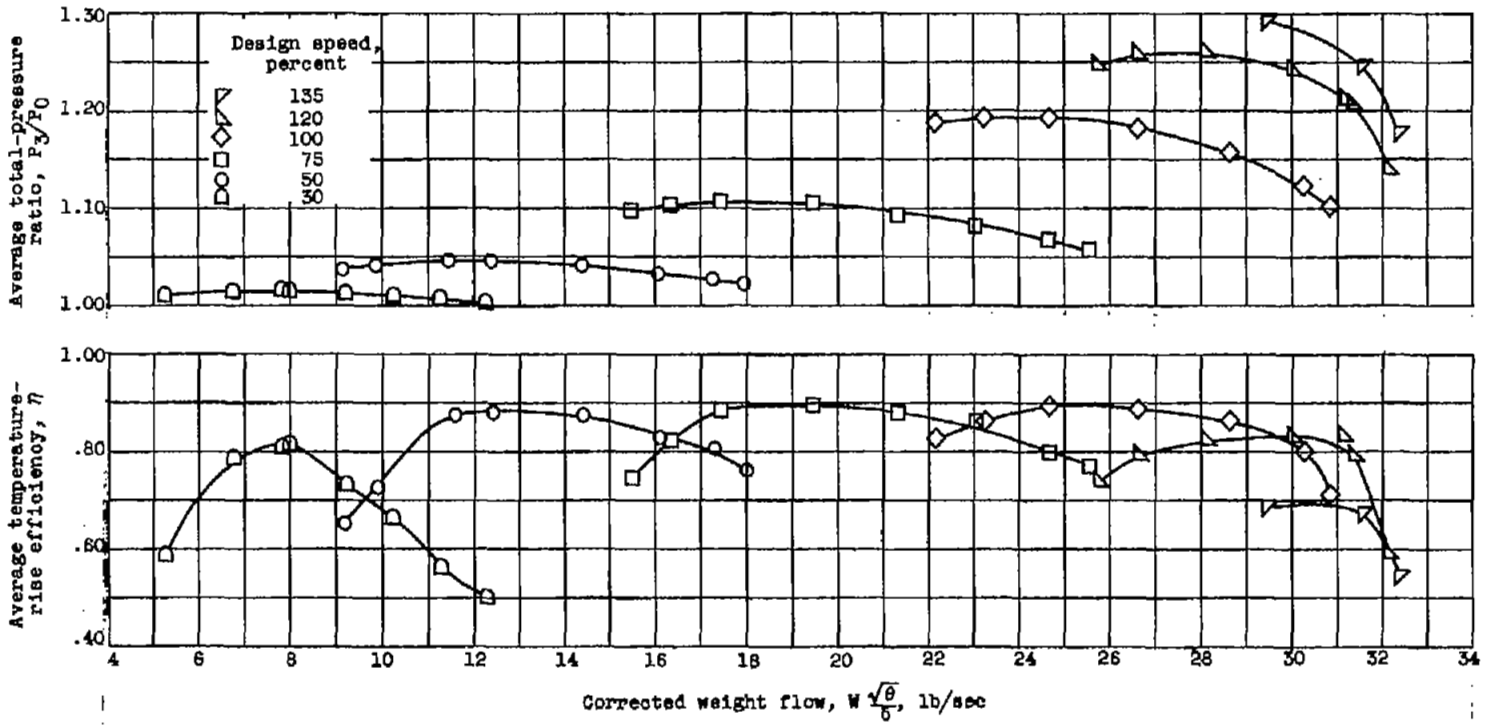

(c) Design 3; design corrected tip speed, $U_t/\sqrt{\theta}$, 823 feet per second.

Figure 5. - Continued. Over-all performance of four axial-flow compressors having a hub-tip radius ratio of 0.5. Full-stage investigation.

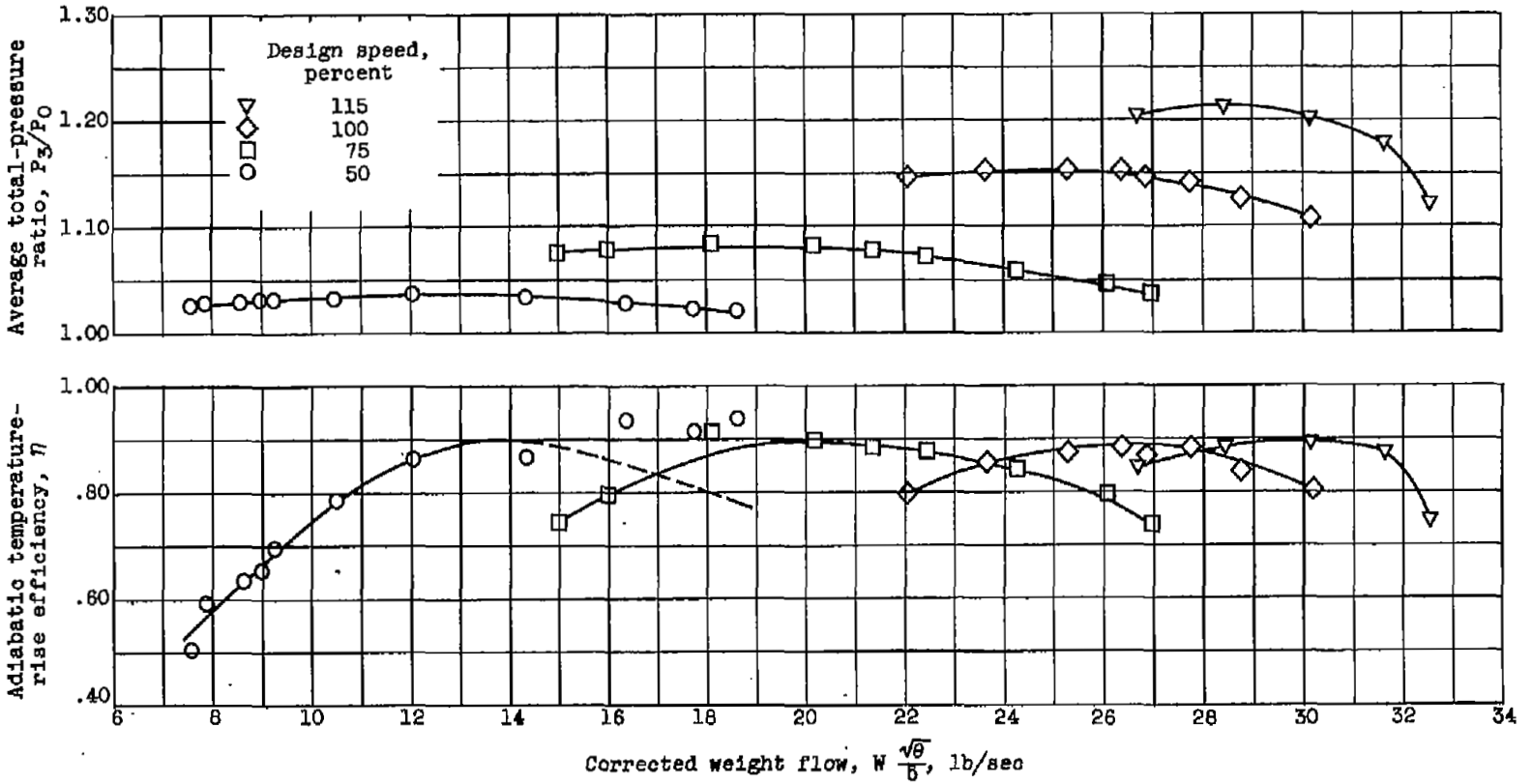

(d) Design 4; design corrected tip speed, $U_t/\sqrt{\theta}$, 743 feet per second.

Figure 5. - Concluded. Over-all performance of four axial-flow compressors having a hub-tip radius ratio of 0.5. Full-stage investigation.

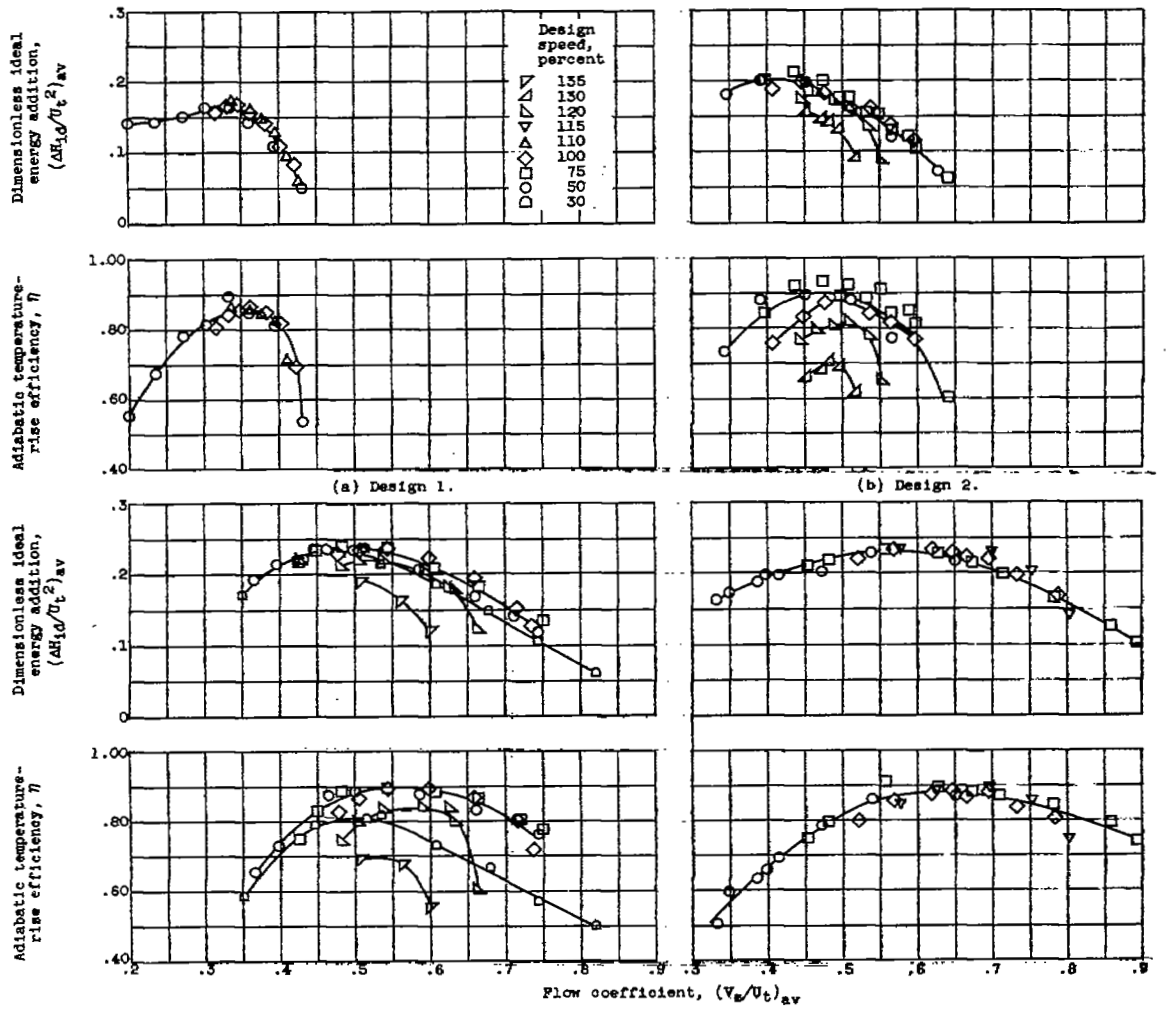

Figure 6. - Dimensionless over-all performance of four axial-flow compressors having a hub-tip radius ratio of 0.5

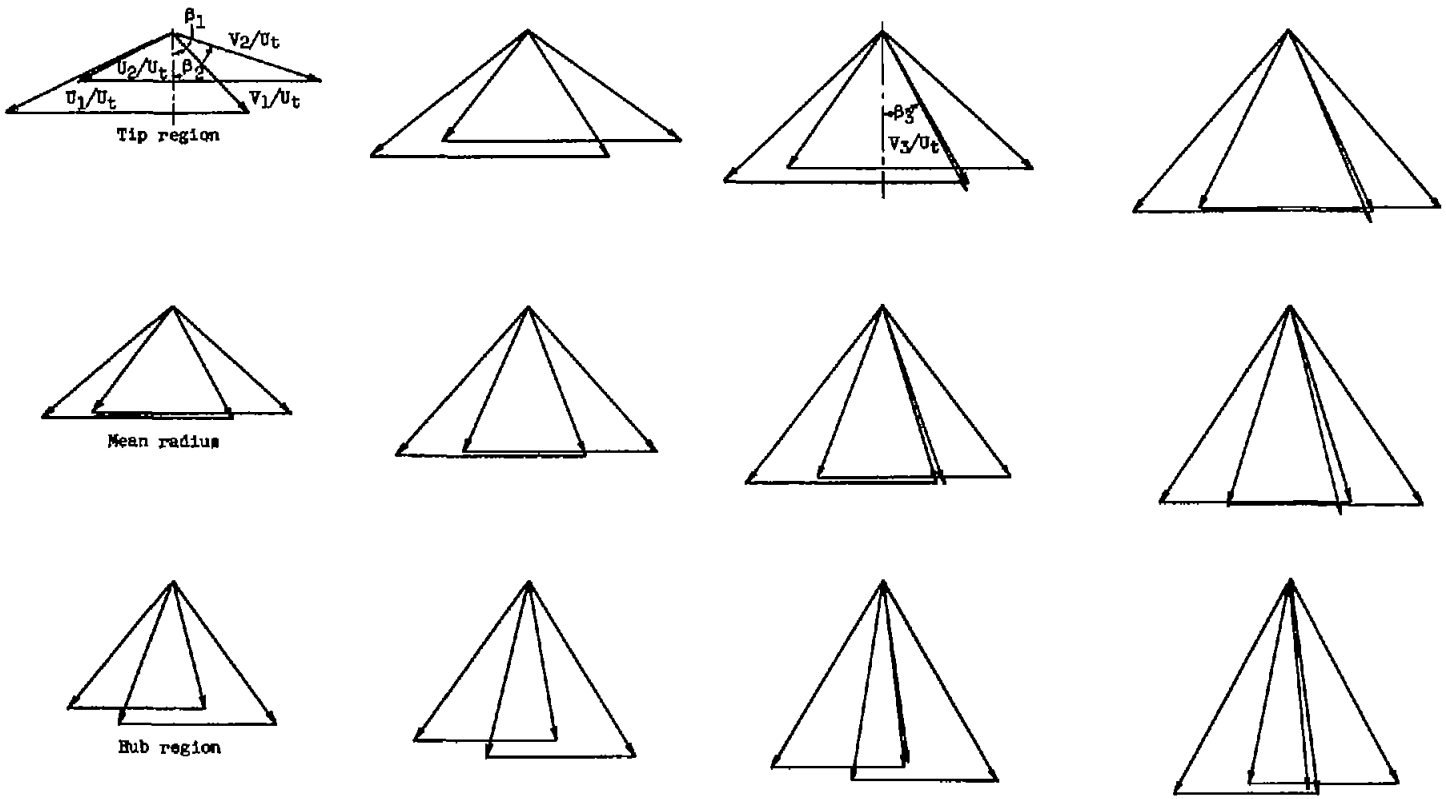

(a) Design 1; no stators; corrected weight flow, $W\sqrt{\theta}/\delta$, 21.51 pounds per second; design corrected tip speed, $U_t/\sqrt{\theta}$, 1104 feet per second.

(b) Design 2; no stators; corrected weight flow, $W\sqrt{\theta}/\delta$, 24.91 pounds per second; design corrected tip speed, $U_t/\sqrt{\theta}$, 938 feet per second.

(c) Design 3; full stage; corrected weight flow, $W\sqrt{\theta}/\delta$, 26.63 pounds per second; design corrected tip speed, $U_t/\sqrt{\theta}$, 823 feet per second.

(d) Design 4; full stage; corrected weight flow, $W\sqrt{\theta}/\delta$, 27.77 pounds per second; design corrected tip speed, $U_t/\sqrt{\theta}$, 745 feet per second.

Figure 7. - Measured velocity diagrams for four axial-flow compressors having a hub-tip radius ratio of 0.5. Peak efficiency point, design speed.

		Design number			
		1	2	3	4
Tip region	V_1/U_t	0.410	0.551	0.640	0.730
	V_2/U_t	0.611	0.722	0.766	0.869
	V_3/U_t			0.667	0.769
	β_1, deg	45.75	34.75	31.0	26.10
	β_2, deg	72.90	56.16	49.32	42.12
	β_3, deg			30.85	24.48
	U_1/U_t	0.950	0.936	0.962	0.939
	U_2/U_t	0.958	0.942	0.965	0.942
Mean radius	V_1/U_t	0.461	0.584	0.668	0.758
	V_2/U_t	0.602	0.736	0.808	0.893
	V_3/U_t			0.690	0.787
	β_1, deg	29.52	22.80	18.04	18.54
	β_2, deg	50.04	43.88	38.88	35.46
	β_3, deg			20.05	14.76
	U_1/U_t	0.746	0.746	0.749	0.749
	U_2/U_t	0.786	0.767	0.766	0.762
Hub region	V_1/U_t	0.475	0.589	0.680	0.781
	V_2/U_t	0.657	0.763	0.852	0.852
	V_3/U_t			0.670	0.767
	β_1, deg	15.12	10.85	7.24	7.92
	β_2, deg	37.80	33.66	31.32	29.52
	β_3, deg			7.99	5.04
	U_1/U_t	0.542	0.557	0.536	0.560
	U_2/U_t	0.615	0.590	0.567	0.584

(e) Tabulated values of velocities and flow angles.

Figure 7. - Concluded. Measured velocity diagrams for four axial-flow compressors having a hub-tip radius ratio of 0.5. Peak efficiency point, design speed.

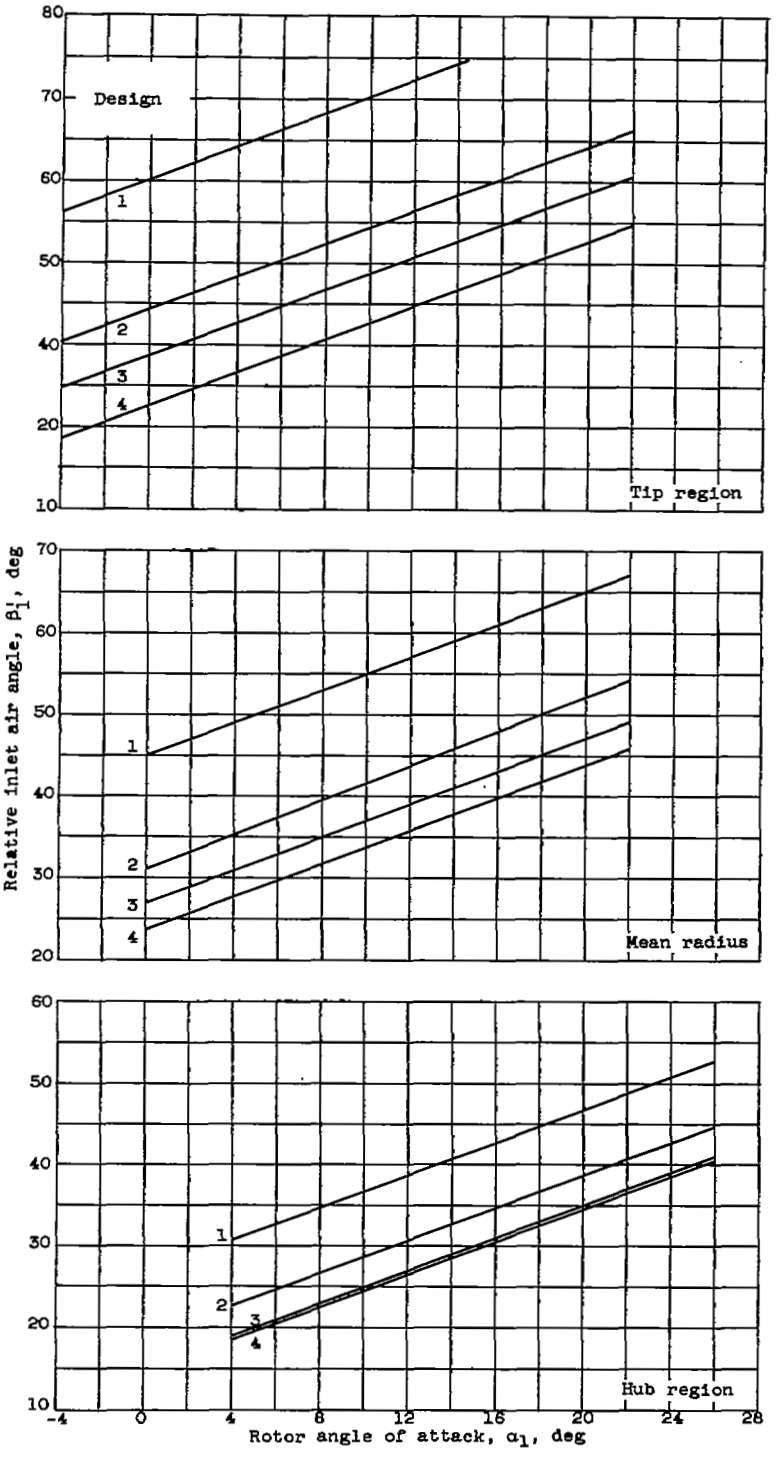

Figure 8. - Variation of relative inlet air angle with rotor angle of attack for four axial-flow compressors having a hub-tip radius ratio of 0.5.

[redacted]

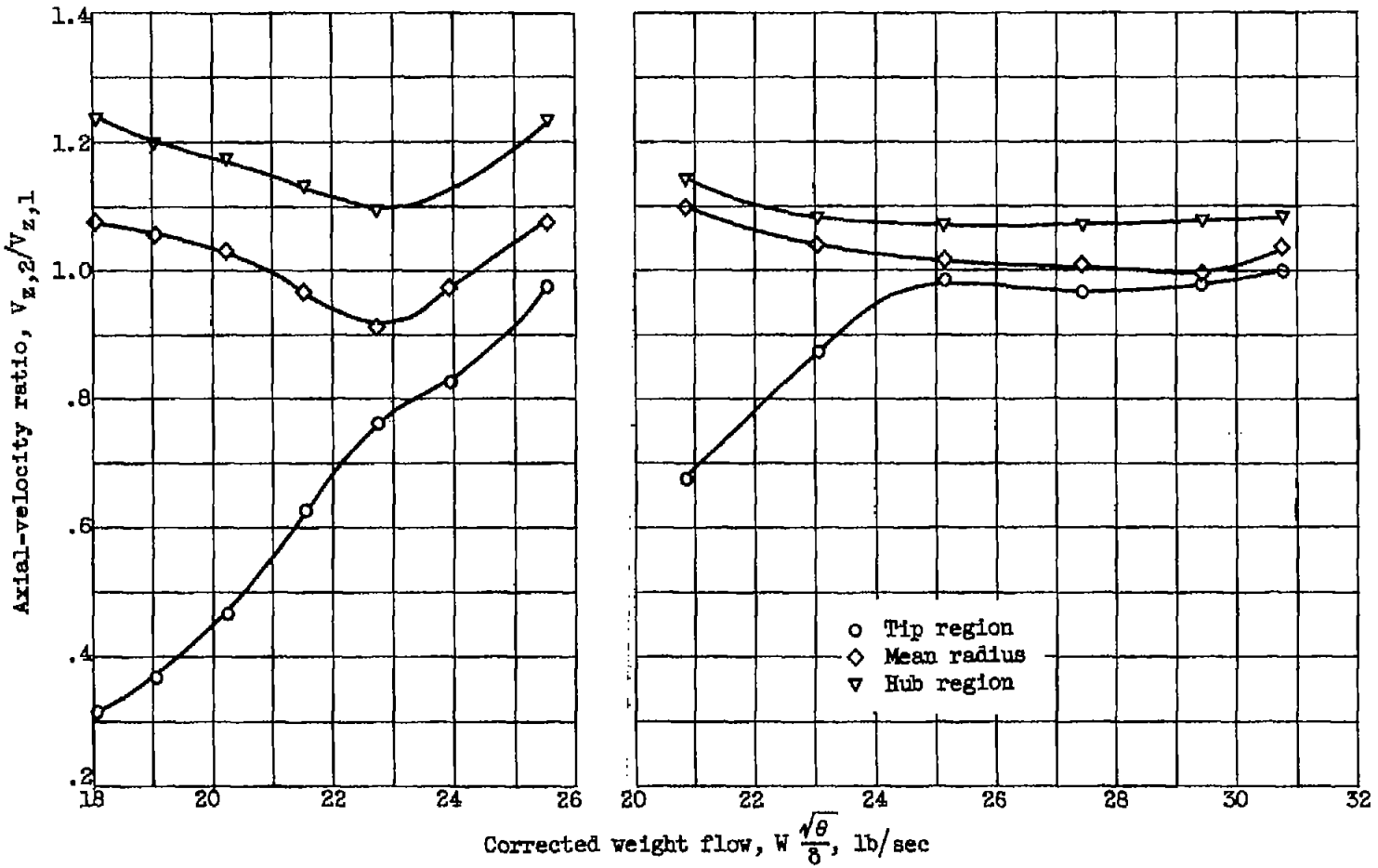

(a) Design 1; rotor investigation; design corrected tip speed, $U_t/\sqrt{\theta}$, 1104 feet per second.

(b) Design 4; rotor investigation; design corrected tip speed, $U_t/\sqrt{\theta}$, 743 feet per second.

Figure 9. - Axial-velocity ratios for two axial-flow compressors having a hub-tip radius ratio of 0.5.

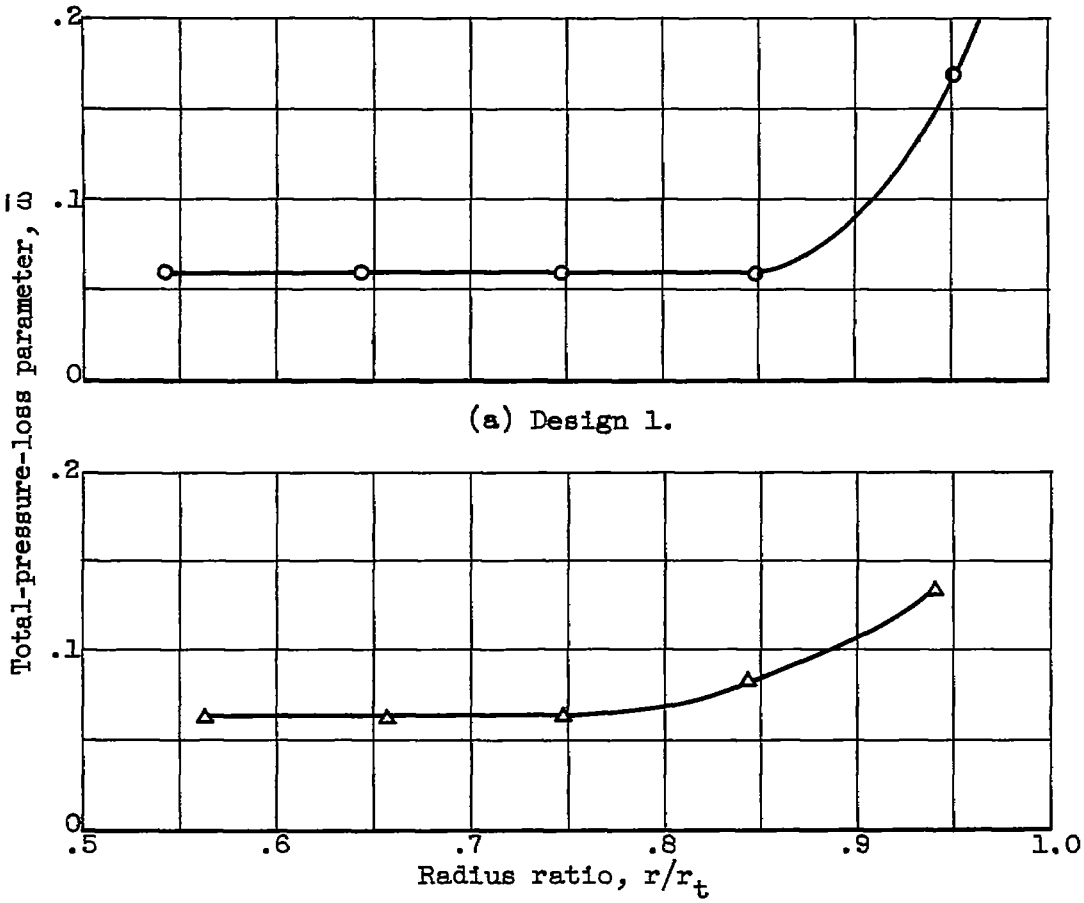

(a) Design 1.

(b) Design 4.

Figure 10. - Guide-vane losses for two axial-flow compressors having a hub-tip radius ratio of 0.5.

[redacted]

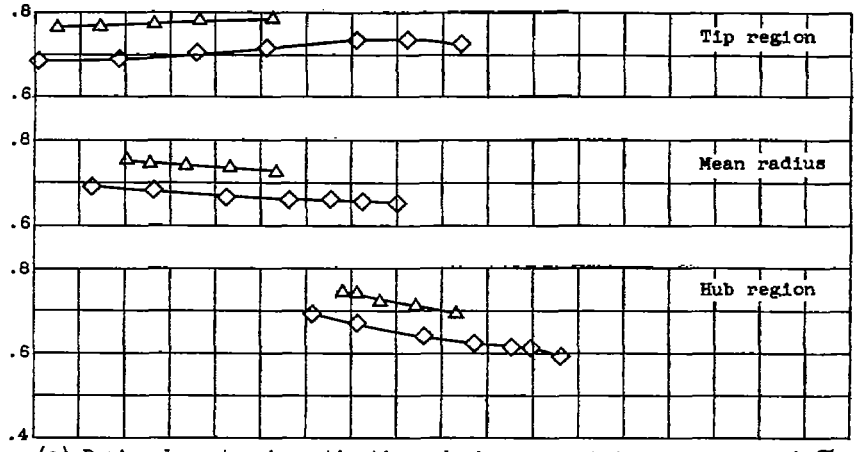

(a) Design 1; rotor investigation; design corrected tip speed, $U_t/\sqrt{\theta}$, 1104 feet per second

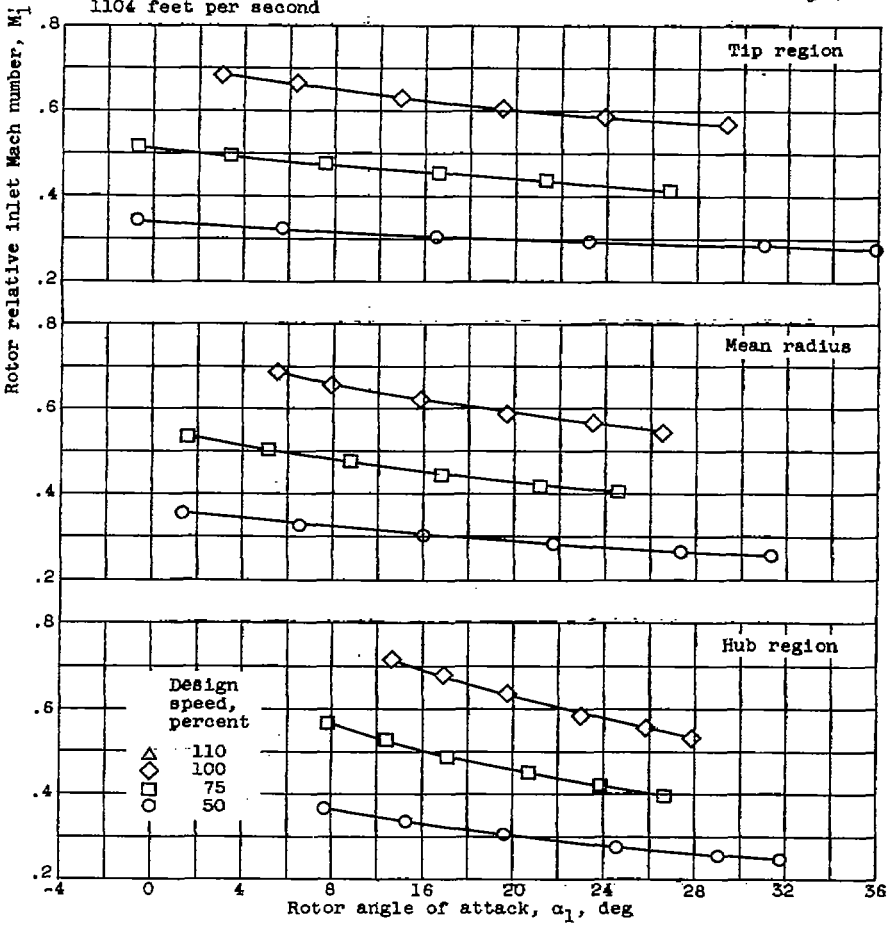

(b) Design 4; rotor investigation; design corrected tip speed, $U_t/\sqrt{\theta}$, 743 feet per second.

Figure 11. - Variation of relative Mach number with rotor angle of attack for two axial-flow compressors having a hub-tip radius ratio of 0.5.

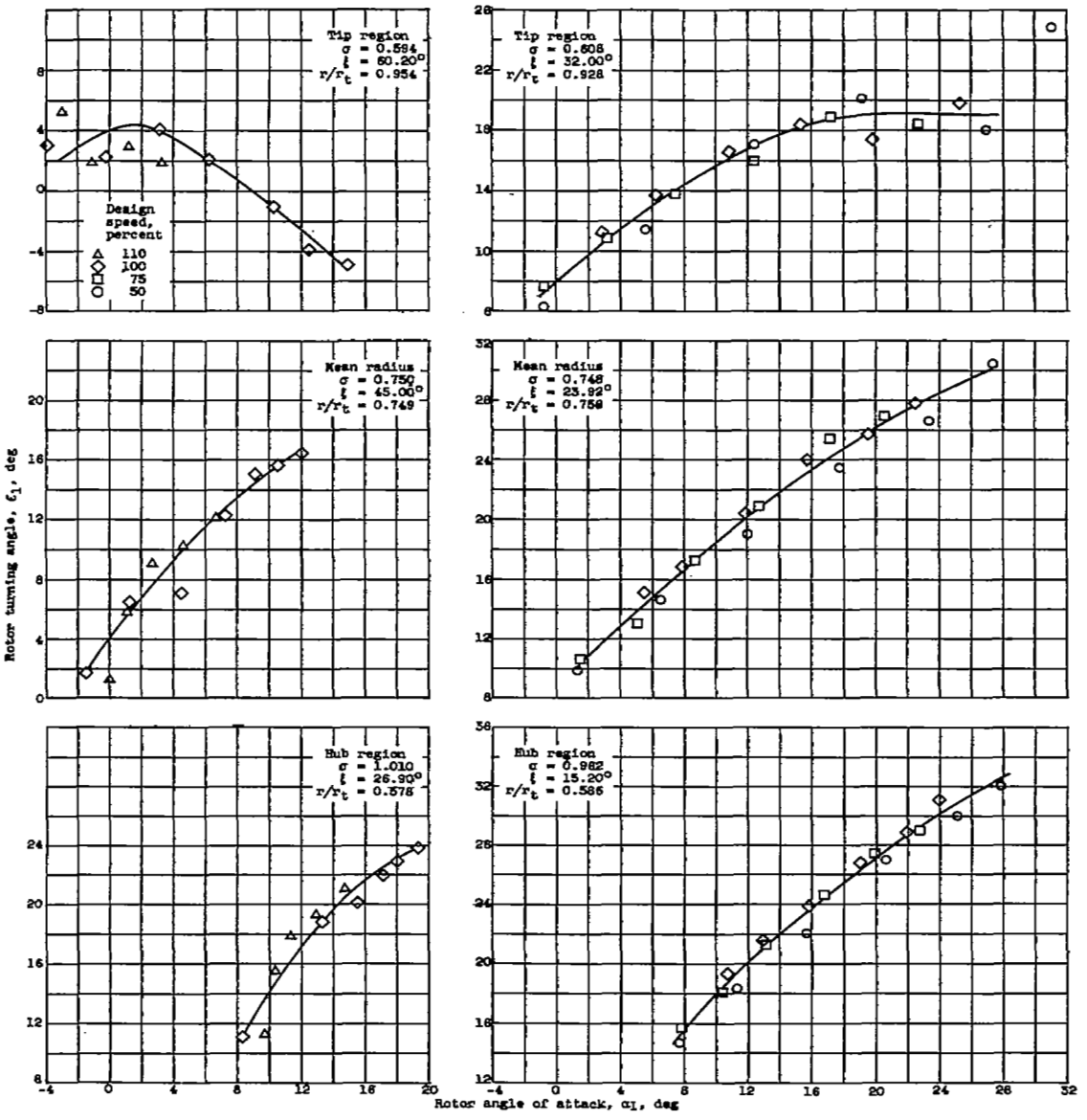

(a) Design 1; rotor investigation; 65-(12)10 blade section; design corrected tip speed, $U_t/\sqrt{\theta}$, 1104 feet per second.

(b) Design 4; rotor investigation; 65-(12)10 blade section; design corrected tip speed, $U_t/\sqrt{\theta}$, 743 feet per second.

Figure 12. - Variation of rotor turning angle with angle of attack for two axial-flow compressors having a hub-tip radius ratio of 0.5.

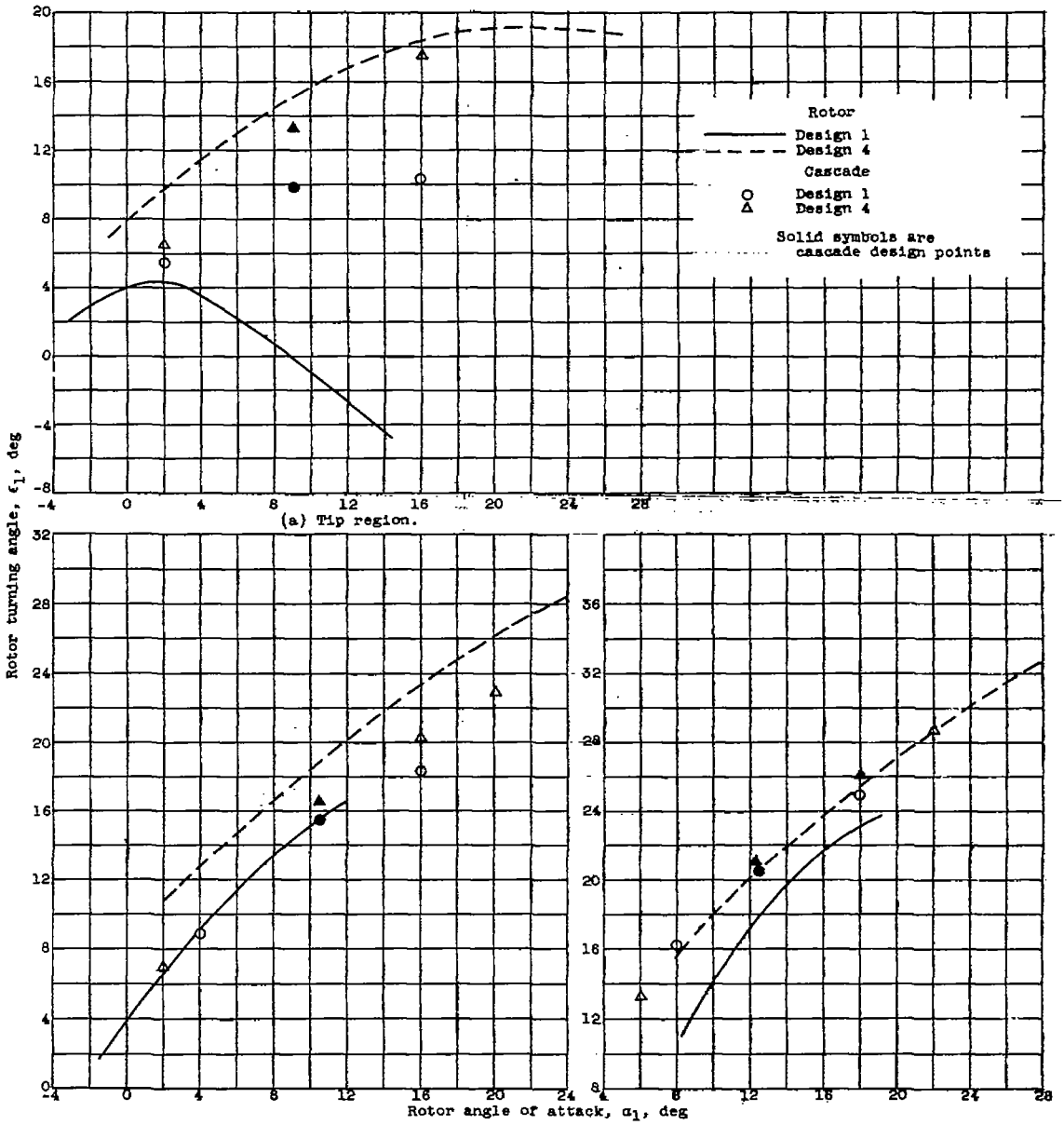

Figure 13. - Comparison of rotor and cascade-predicted turning angles for two axial-flow compressors having a hub-tip radius ratio of 0.5.

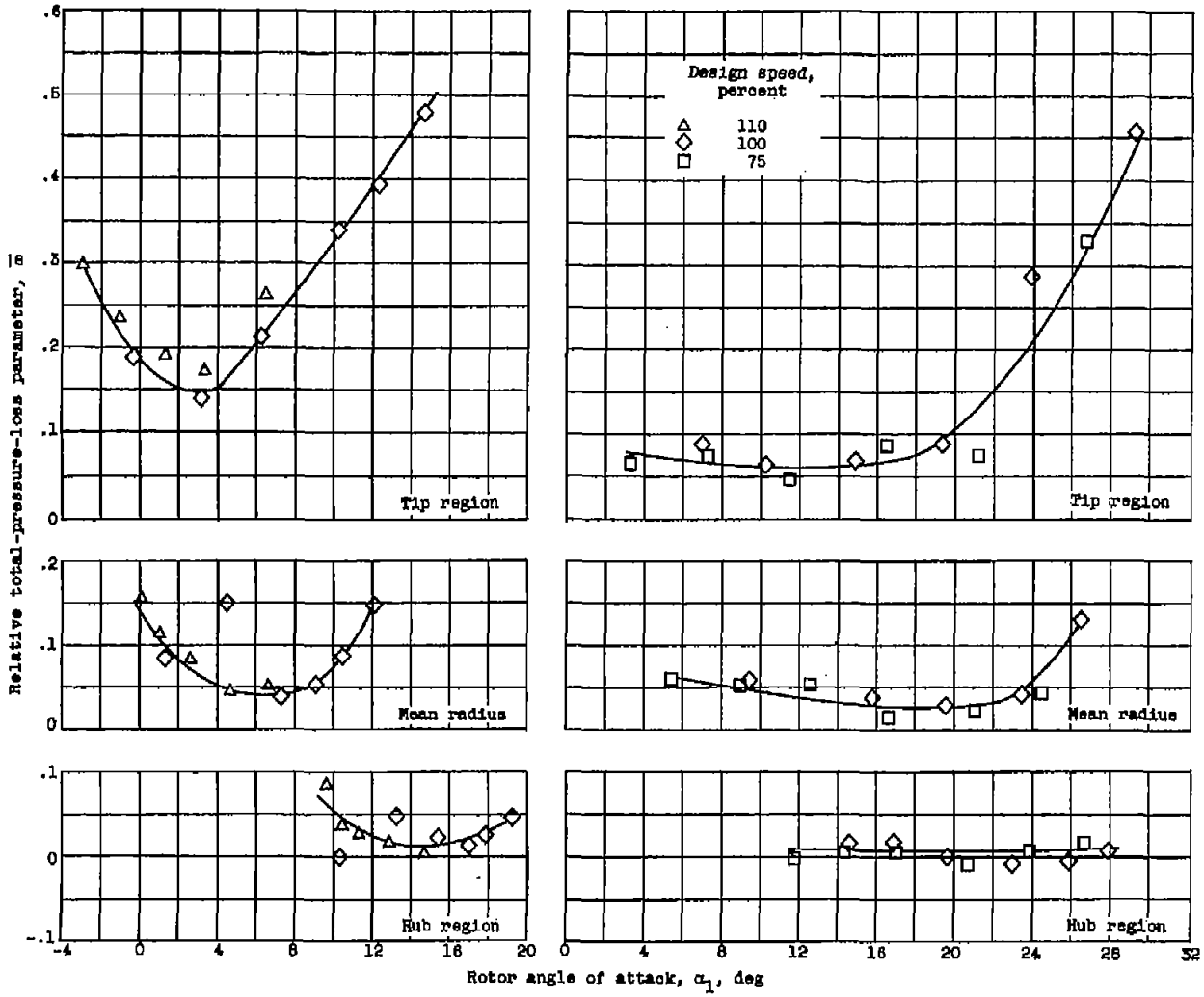

(a) Design 1; rotor investigation; design corrected tip speed, $U_t/\sqrt{\theta}$, 1104 feet per second.

(b) Design 4; rotor investigation; design corrected tip speed, $U_t/\sqrt{\theta}$, 743 feet per second.

Figure 14. - Rotor total-pressure losses for two axial-flow compressors having a hub-tip radius ratio of 0.5.

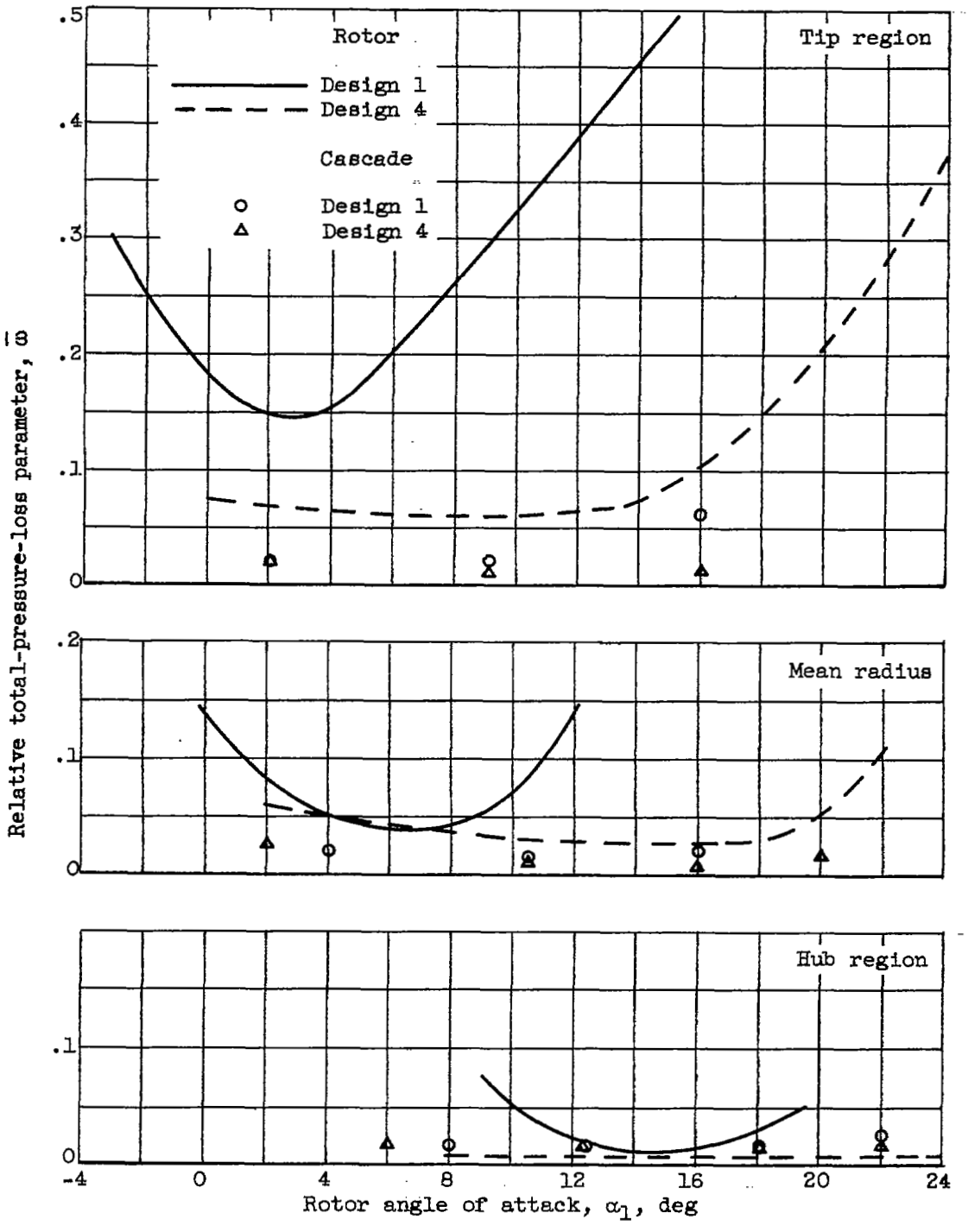

Figure 15. - Comparison of rotor and cascade-predicted losses for two axial-flow compressors having a hub-tip radius ratio of 0.5.

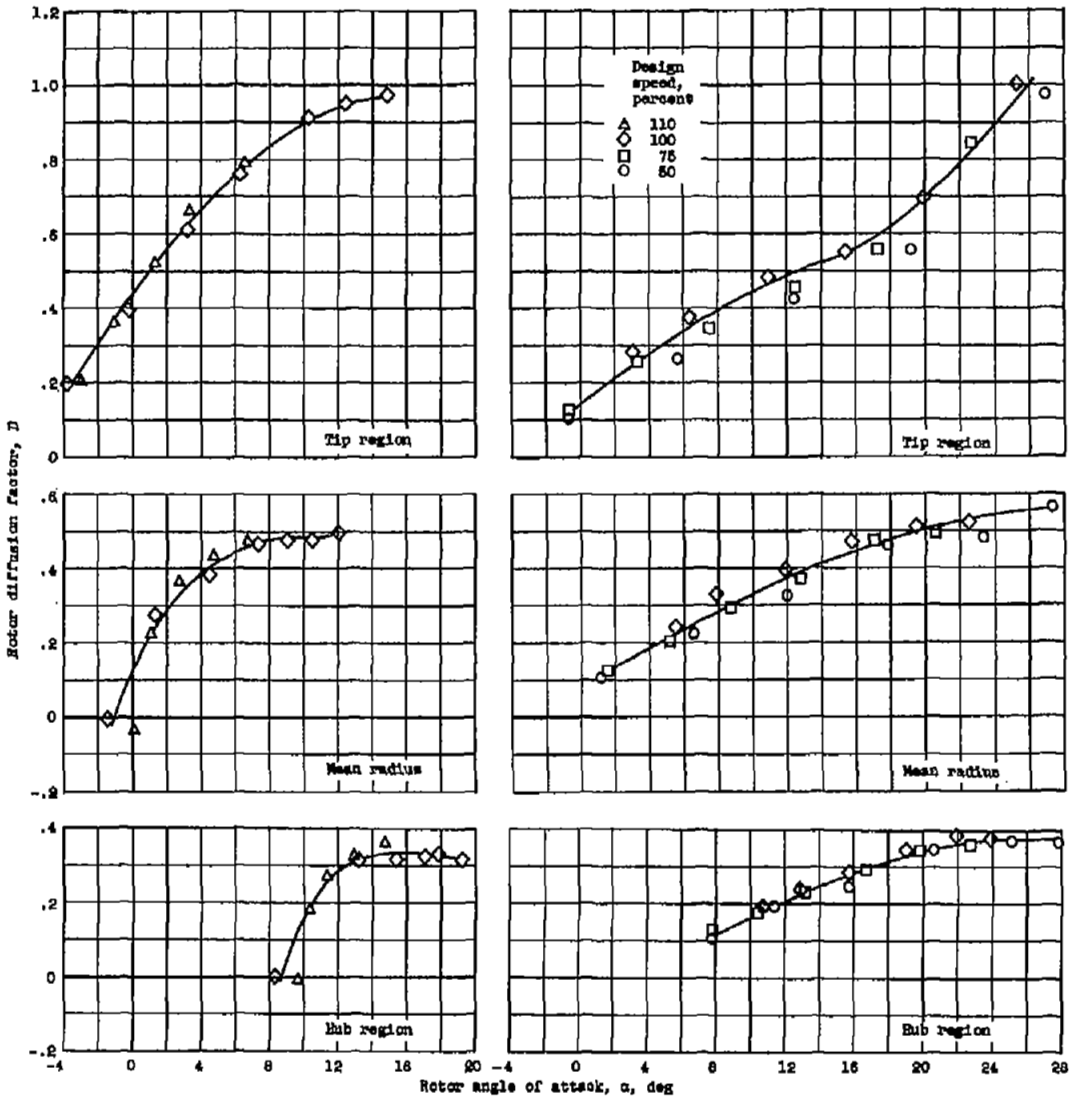

(a) Design 1; rotor investigation; design corrected tip speed, $U_t/\sqrt{\theta}$, 1104 feet per second.

(b) Design 4; rotor investigation; design corrected tip speed, $U_t/\sqrt{\theta}$, 745 feet per second.

Figure 16. - Rotor diffusion factors for two axial-flow compressors having a hub-tip radius ratio of 0.5.

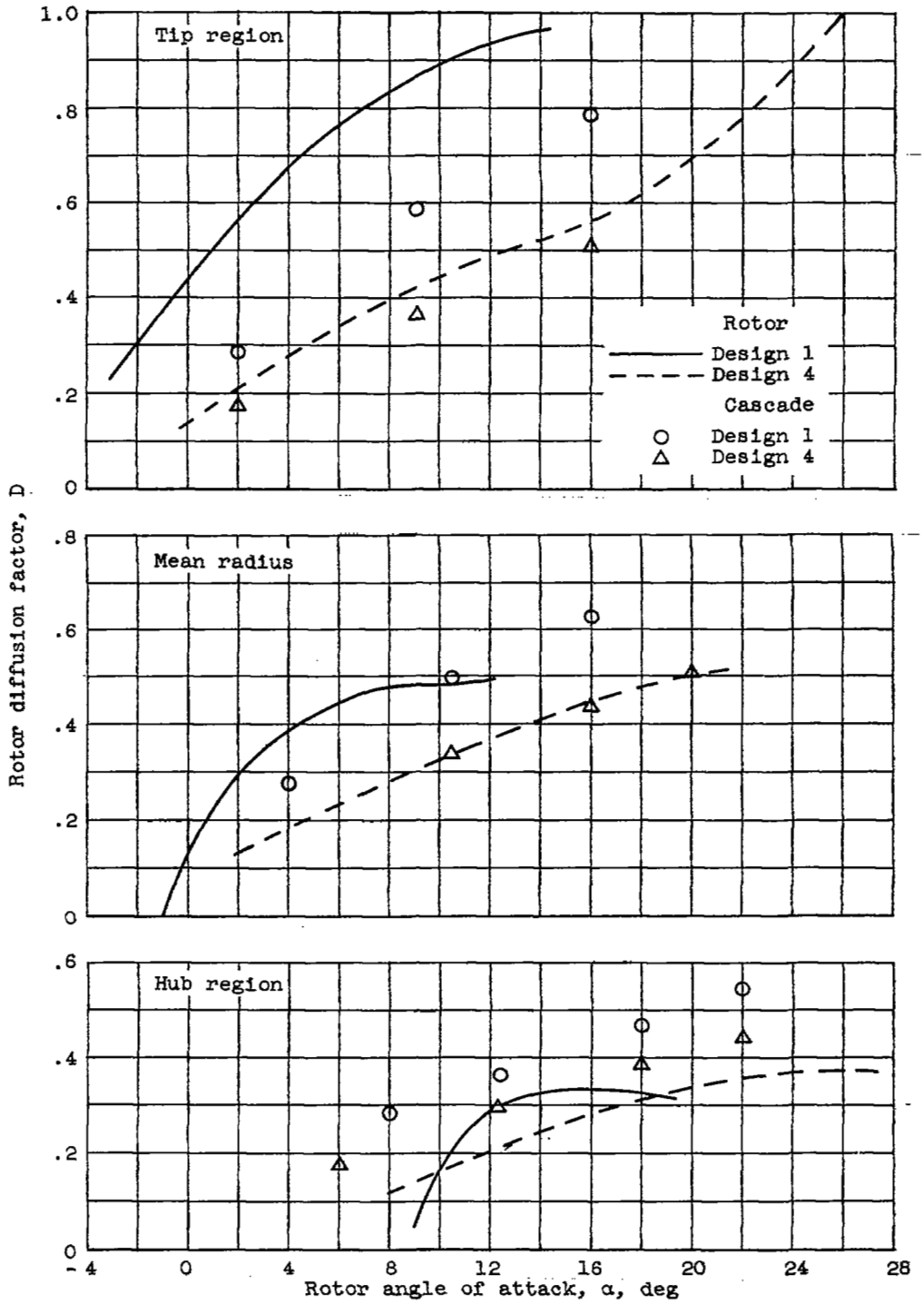

Figure 17. - Comparison of rotor and cascade-predicted diffusion factors for two axial-flow compressors having a hub-tip radius ratio of 0.5.

[redacted]

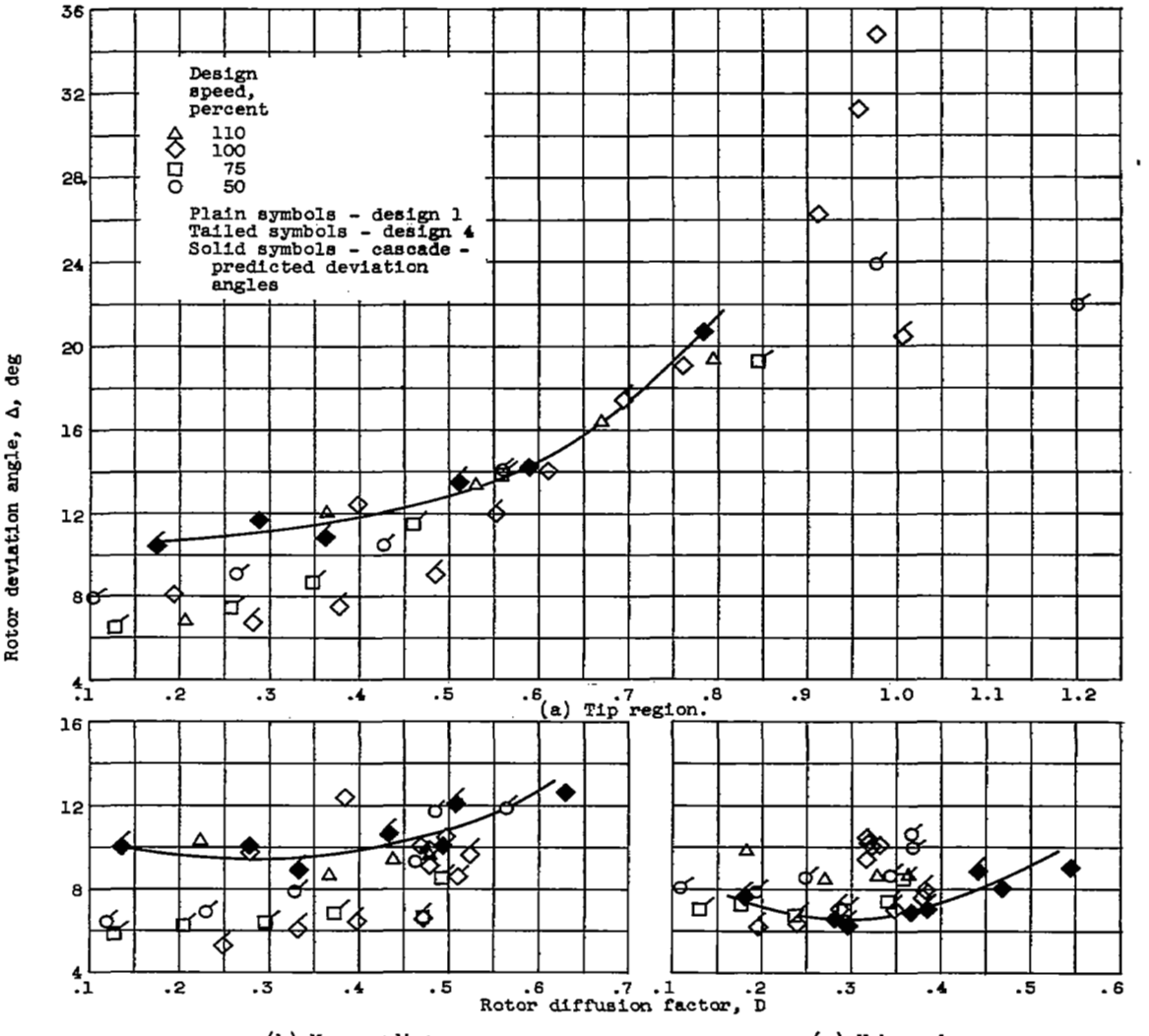

Figure 18. - Variation of rotor deviation angles with diffusion factor for two axial-flow compressors having a hub-tip radius ratio of 0.5.

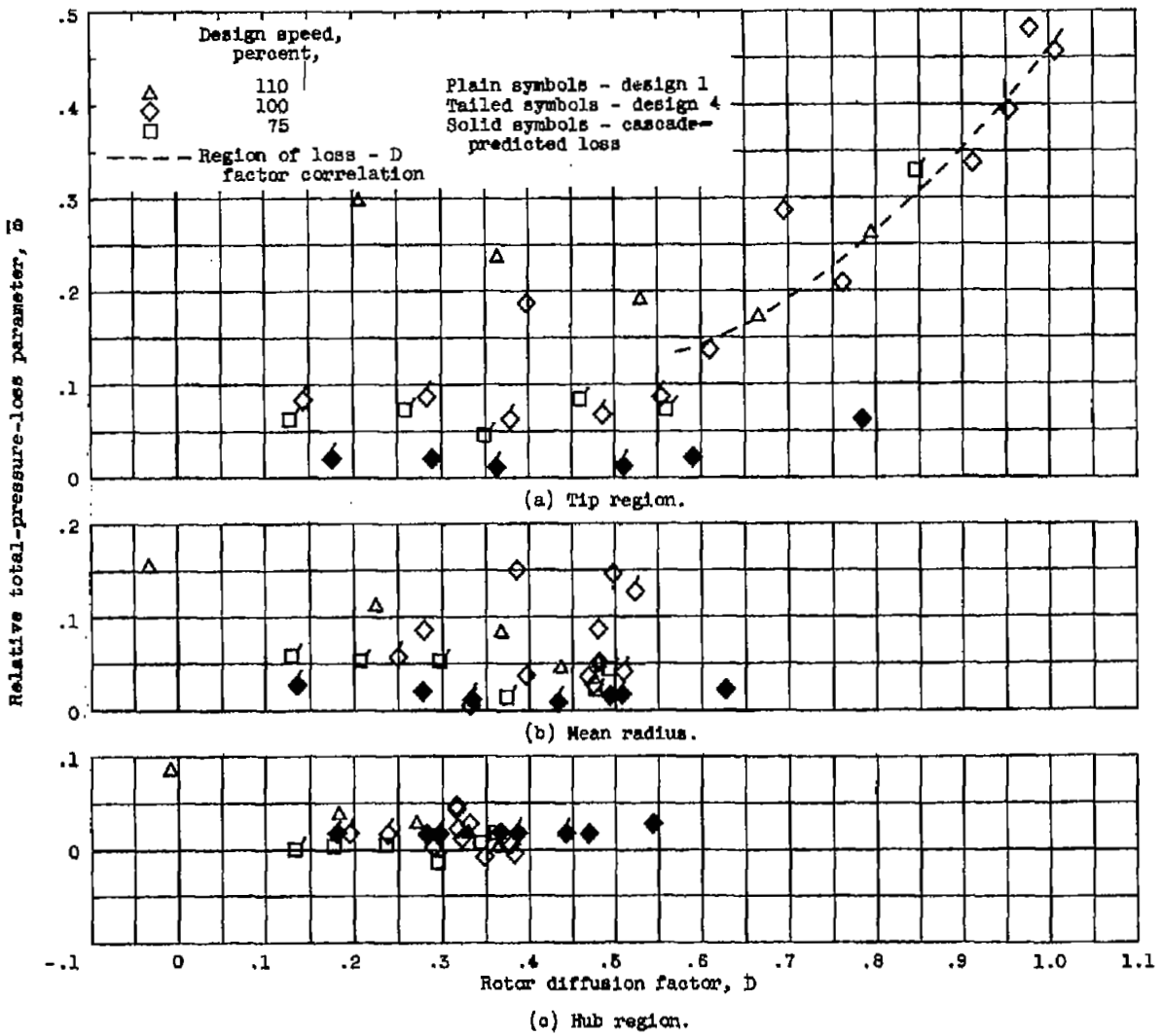

Figure 19. - Variation of rotor loss parameter with diffusion factor for two axial-flow compressors having a hub-tip radius ratio of 0.5.

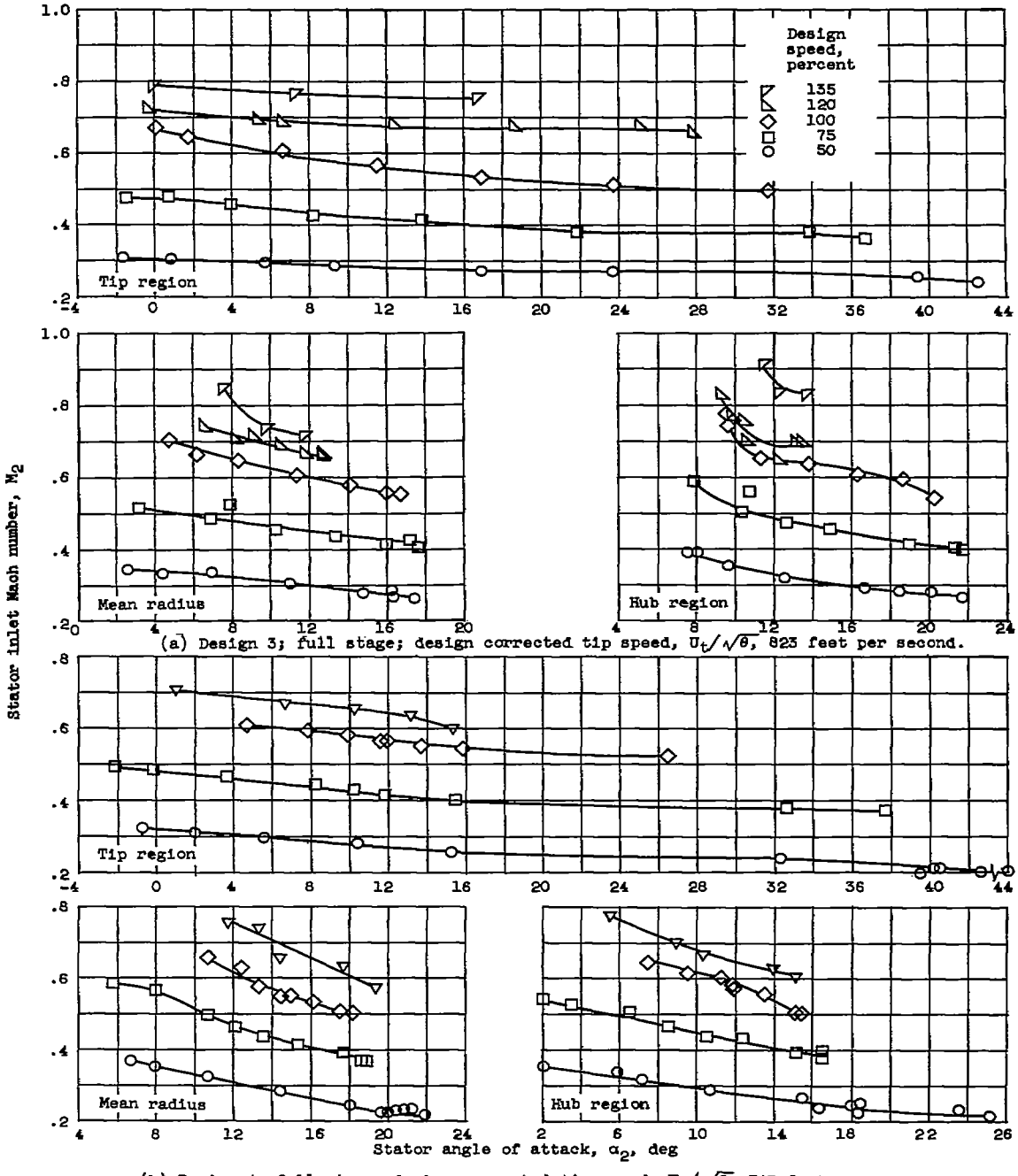

(a) Design 3; full stage; design corrected tip speed, $U_t/\sqrt{\theta}$, 823 feet per second.

(b) Design 4; full stage; design corrected tip speed, $U_t/\sqrt{\theta}$, 743 feet per second.

Figure 20. - Variation of Mach number with stator angle of attack for two axial-flow compressors having a hub-tip radius ratio of 0.5.

[redacted]

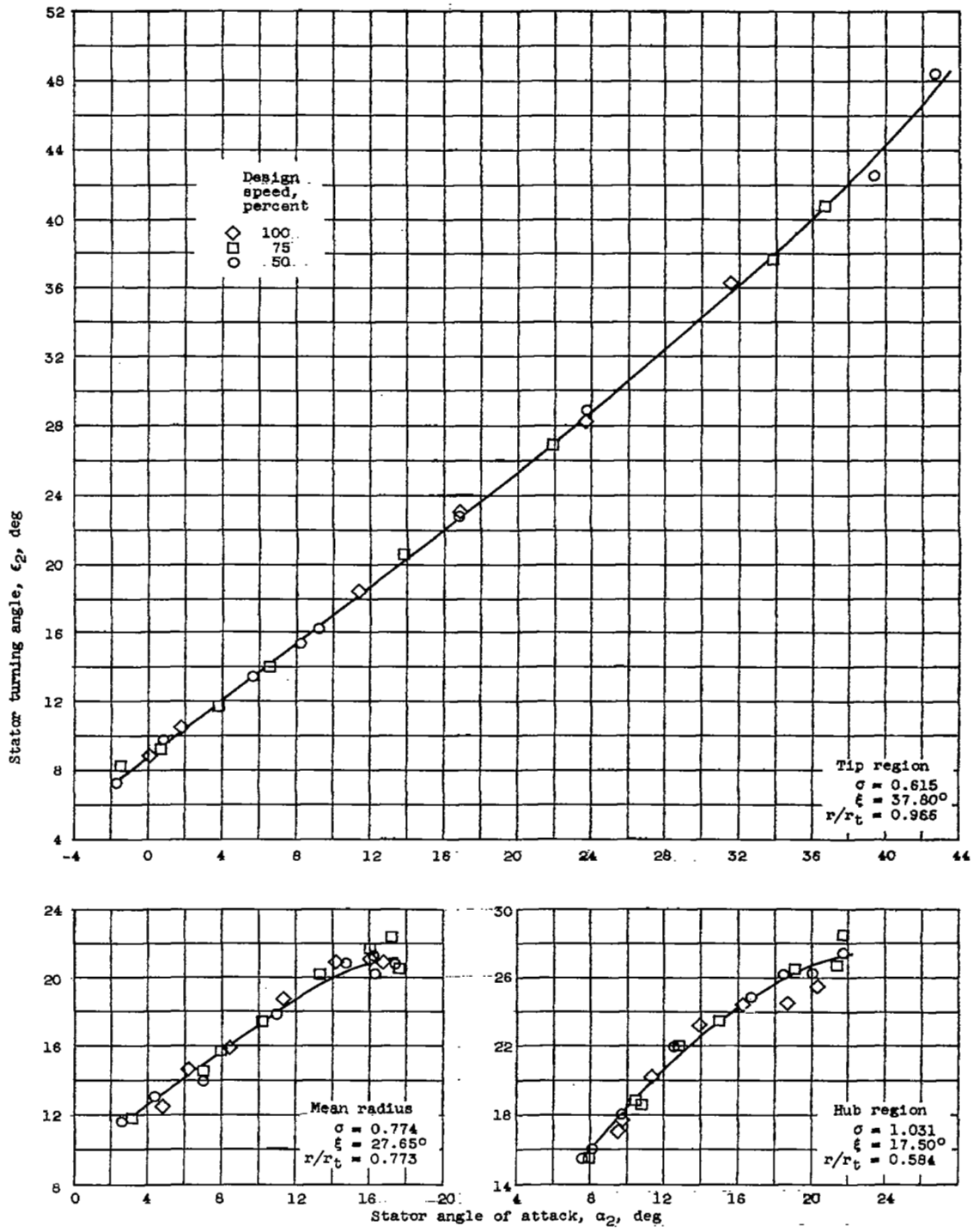

(a) Design 3; design corrected tip speed, $U_t/\sqrt{\theta}$, 823 feet per second.

Figure 21. - Stator turning-angle characteristics for two axial-flow compressors having a hub-tip radius ratio of 0.5.

[redacted]

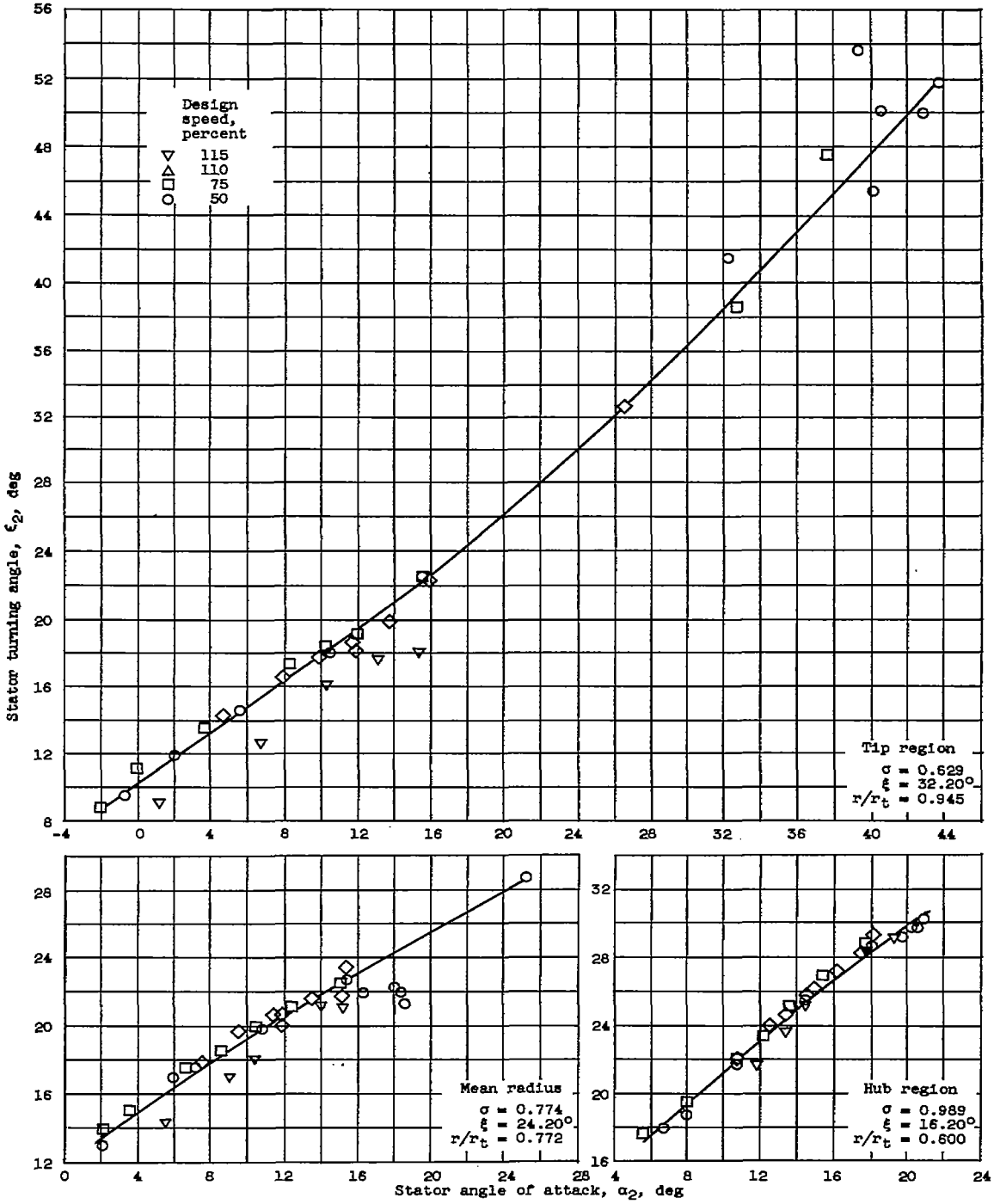

(b) Design 4; design corrected tip speed, $U_t/\sqrt{\theta}$, 743 feet per second.

Figure 21. - Concluded. Stator turning-angle characteristics for two axial-flow compressors having a hub-tip radius ratio of 0.5.

[redacted]

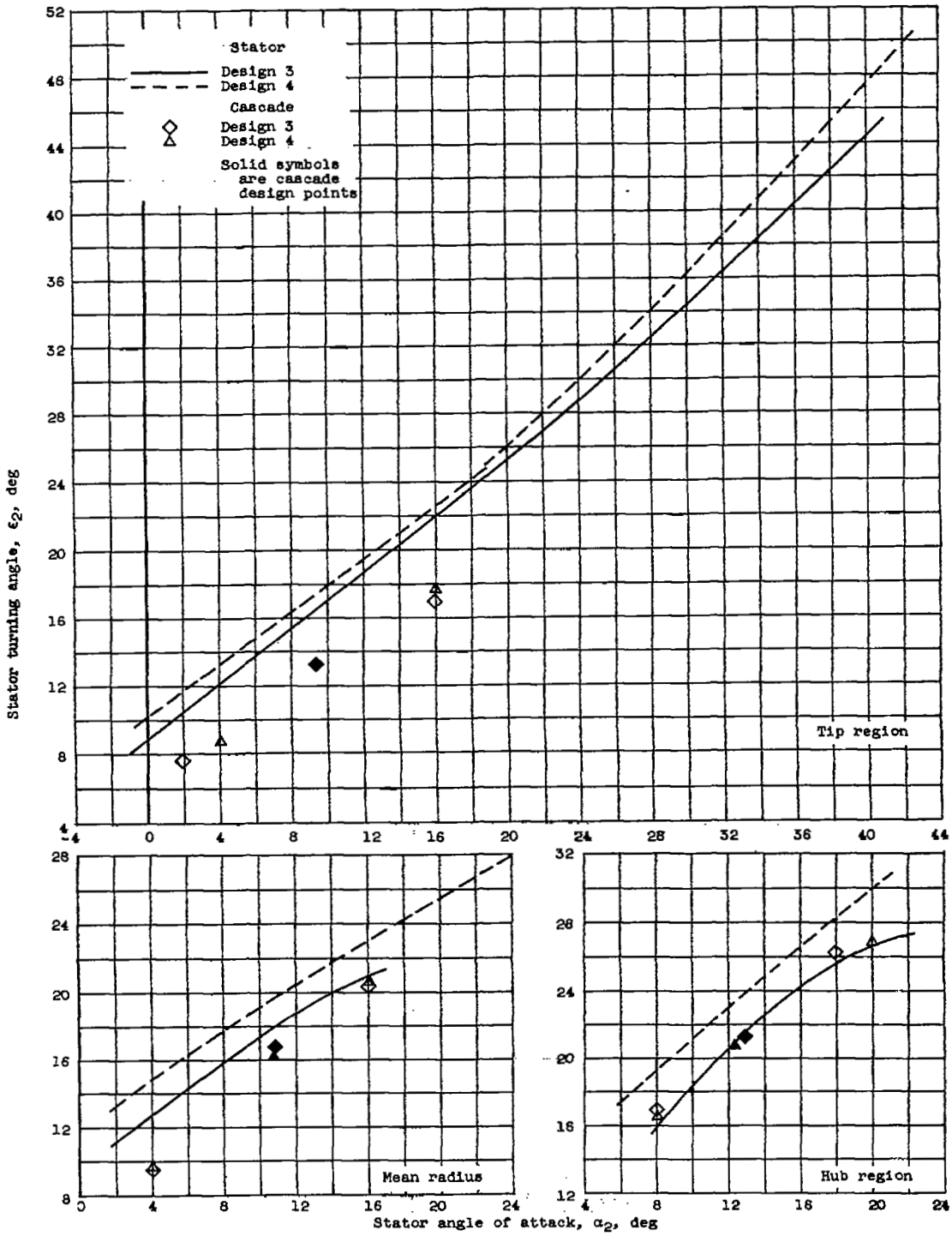

Figure 22. - Comparison of stator and cascade-predicted turning angles for two axial-flow compressors having a hub-tip radius ratio of 0.5.

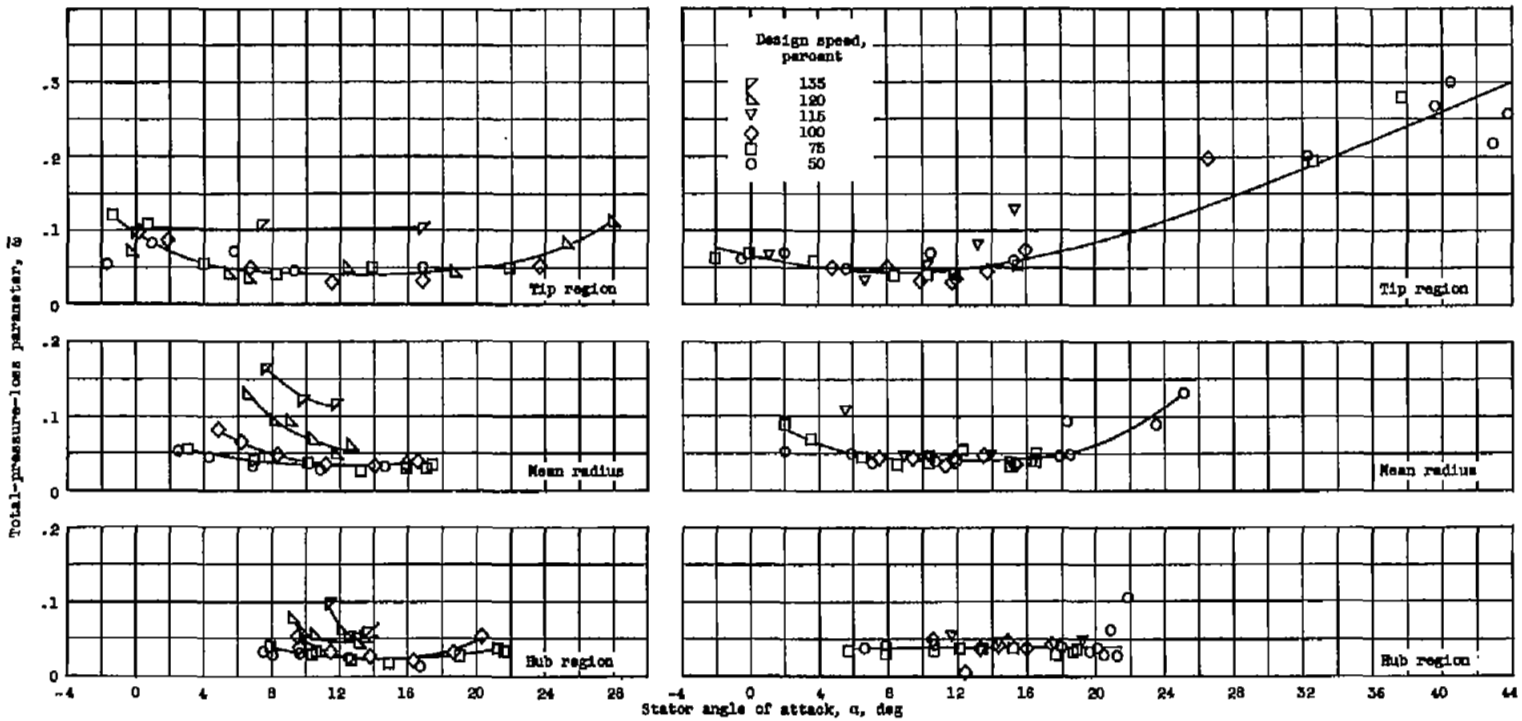

(a) Design 3; full stage; design corrected tip speed, $U_t/\sqrt{\theta}$, 823 feet per second.

(b) Design 4; full stage; design corrected tip speed, $U_t/\sqrt{\theta}$, 743 feet per second.

Figure 23. - Stator total-pressure losses for two axial-flow compressors having a hub-tip radius ratio of 0.5.

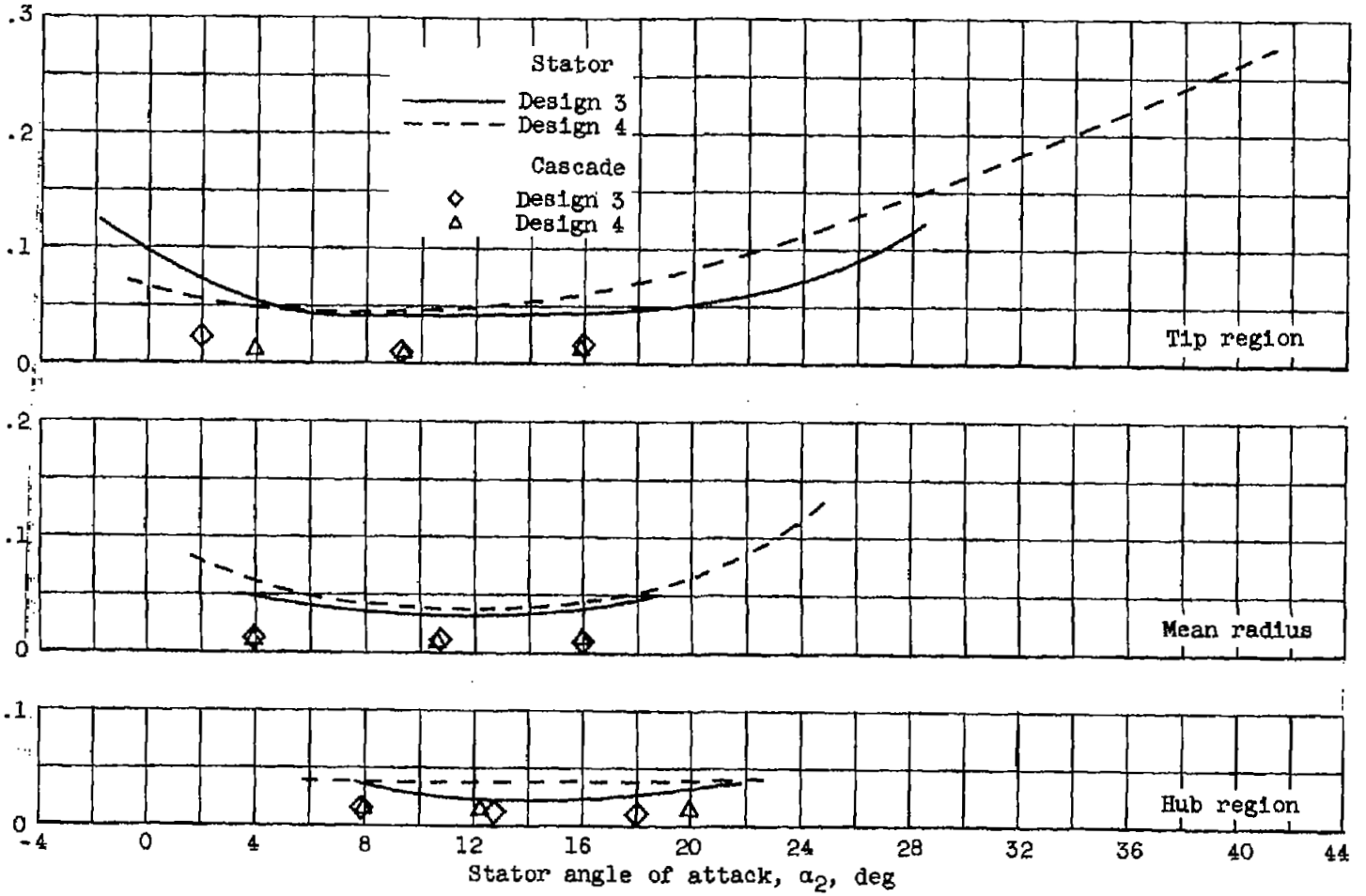

Figure 24. - Comparison of stator and cascade-predicted losses for two axial-flow compressors having a hub-tip radius ratio of 0.5.

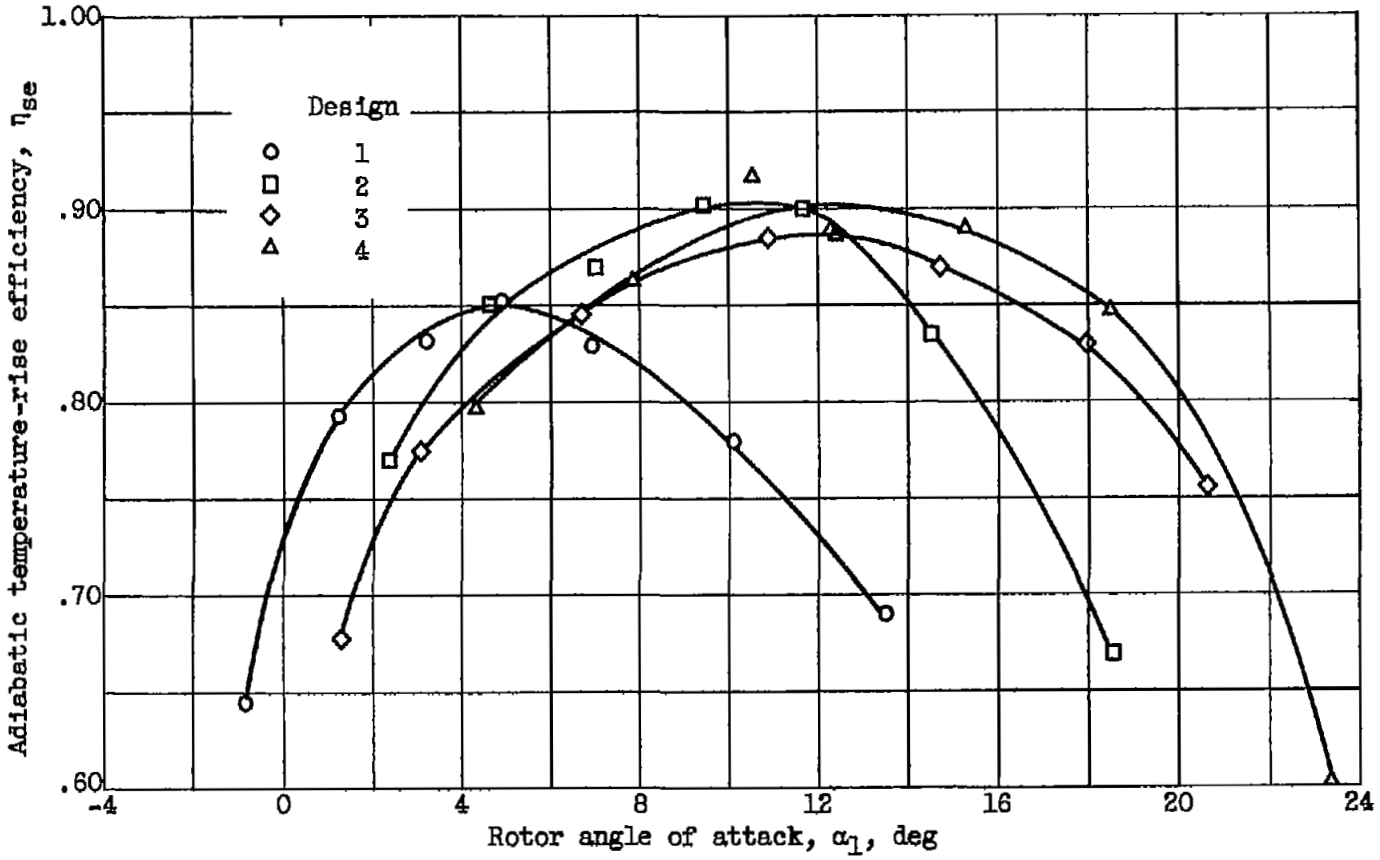

Figure 25. - Comparison of tip-region stage-element efficiencies for two axial-flow compressors having a hub-tip radius ratio of 0.5. Tip region; design corrected tip speed; radius r_3, 0.552 feet.

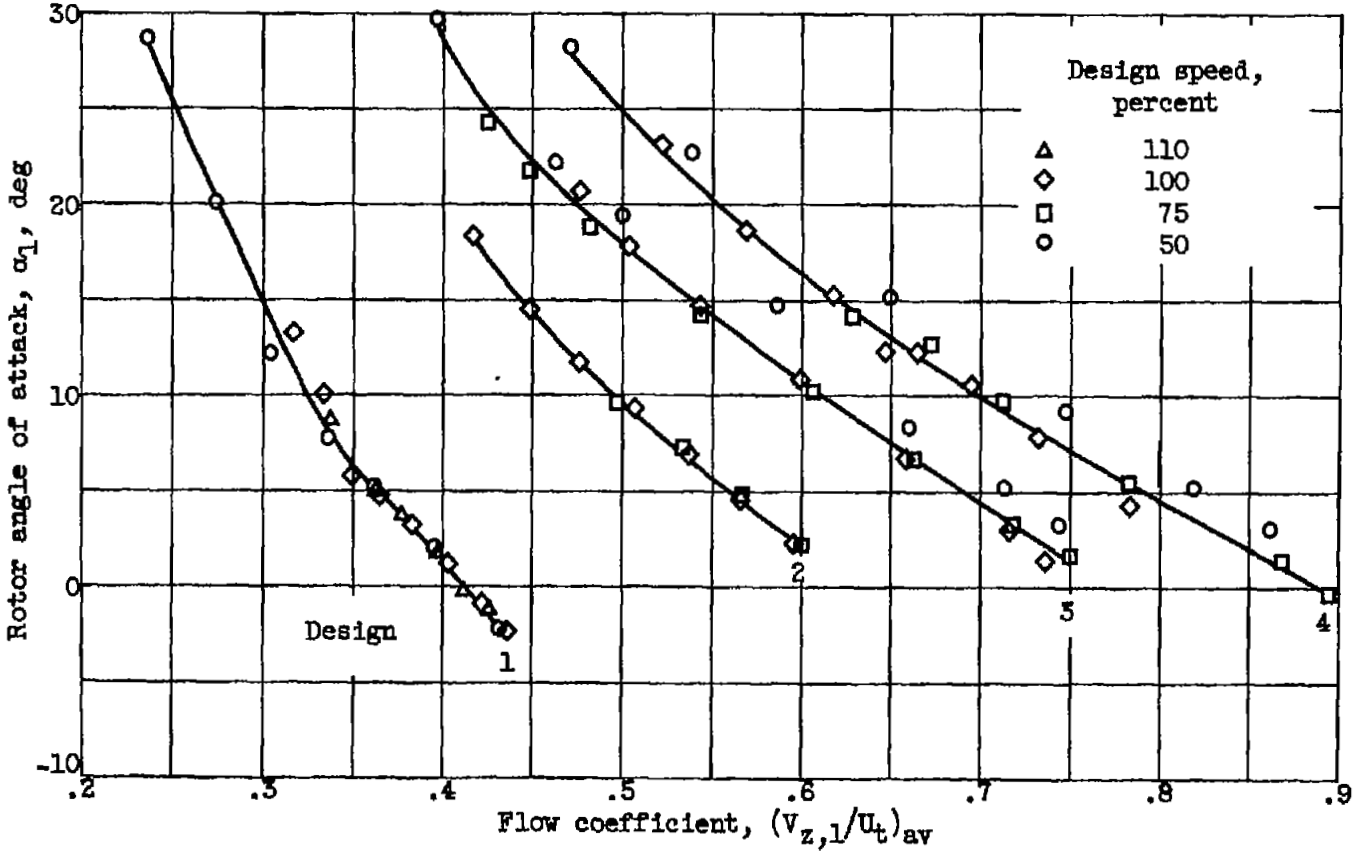

Figure 26. - Comparison of tip-region characteristics of angle of attack against flow coefficient for four axial-flow compressors having a hub-tip radius ratio of 0.5.

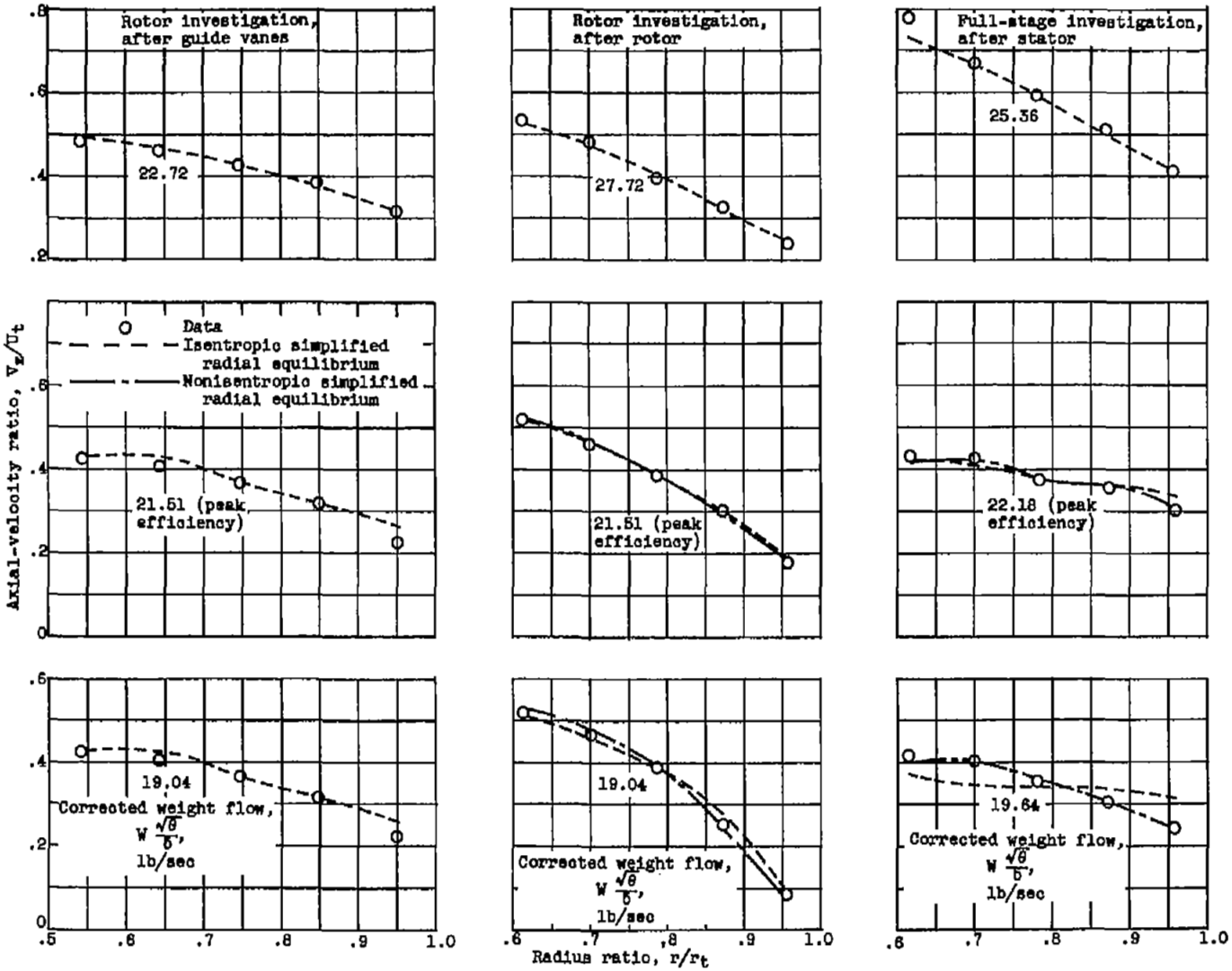

(a) Design 1.

Figure 27. - Radial equilibrium comparison among four axial-flow compressors having a hub-tip radius ratio of 0.5.

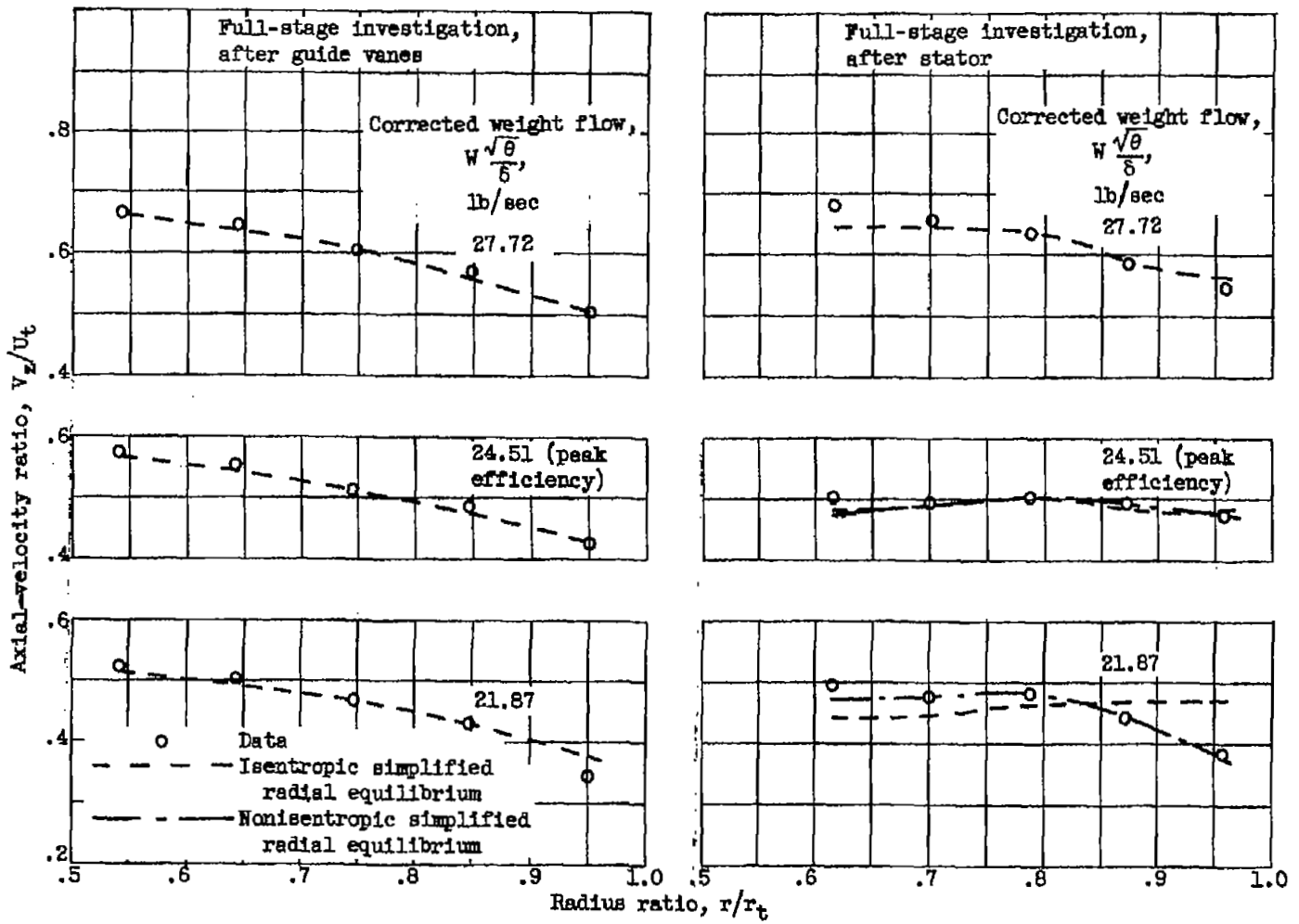

(b) Design number 2.

Figure 27. - Continued. Radial equilibrium comparison among four axial-flow compressors having a hub-tip radius ratio of 0.5.

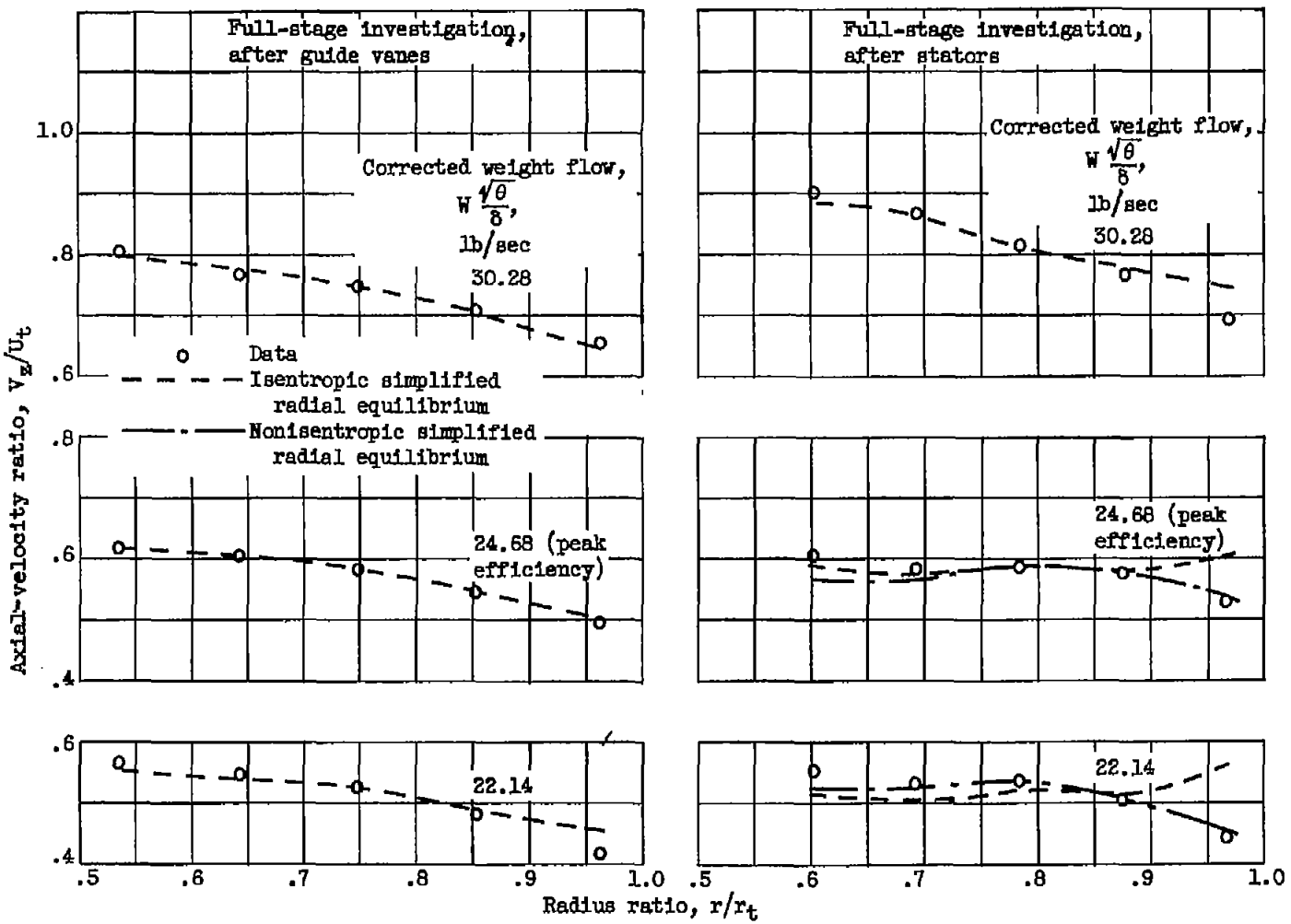

(c) Design 3.

Figure 27. - Continued. Radial equilibrium comparison among four axial-flow compressors having a hub-tip radius ratio of 0.5.

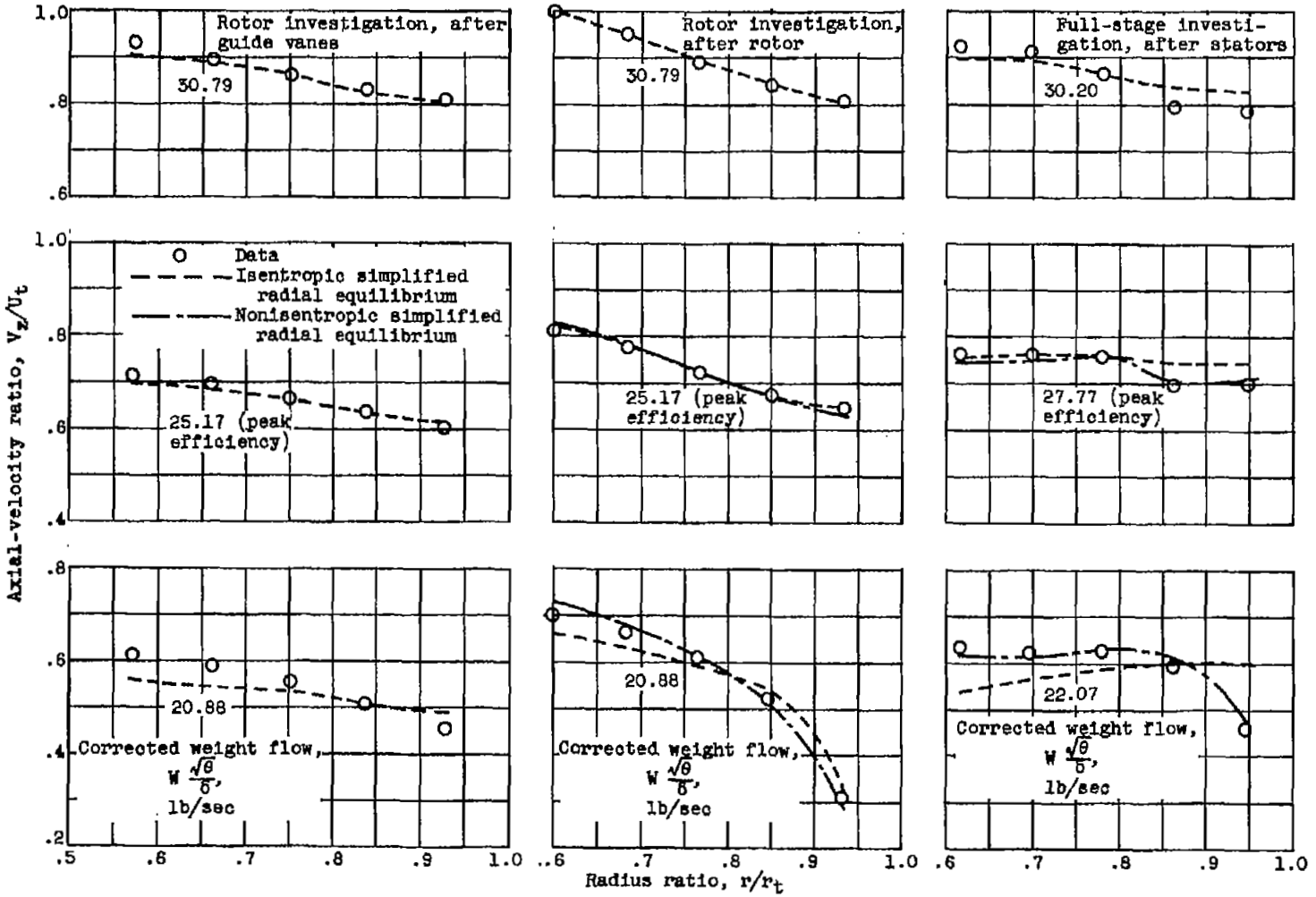

(d) Design 4.

Figure 27. - Concluded. Radial equilibrium comparison among four axial-flow compressors having a hub-tip radius ratio of 0.5.